Influence of ECAP Parameters on the Structural, Electrochemical and Mechanical Behavior of ZK30: A Combination of Experimental and Machine Learning Approaches

Mahmoud Shaban [1,2], Abdulrahman I. Alateyah [3,*], Mohammed F. Alsharekh [1], Majed O. Alawad [4], Amal BaQais [5], Mokhtar Kamel [6], Fahad Nasser Alsunaydih [1], Waleed H. El-Garaihy [3,6,*] and Hanadi G. Salem [7]

1 Department of Electrical Engineering, College of Engineering, Qassim University, Unaizah 56452, Saudi Arabia
2 Department of Electrical Engineering, Faculty of Engineering, Aswan University, Aswan 81542, Egypt
3 Department of Mechanical Engineering, College of Engineering, Qassim University, Unaizah 56452, Saudi Arabia
4 Materials Science Research Institute, King Abdulaziz City for Science and Technology (KACST), Riyadh 12354, Saudi Arabia
5 Department of Chemistry, College of Science, Princess Nourah bint Abdulrahman University, Riyadh 11671, Saudi Arabia
6 Mechanical Engineering Department, Faculty of Engineering, Suez Canal University, Ismailia 41522, Egypt
7 Mechanical Engineering Department, The American University in Cairo, Cairo 11835, Egypt
* Correspondence: a.alateyah@qu.edu.sa (A.I.A.); w.nasr@qu.edu.sa (W.H.E.-G.); Tel.: +966-055-313-3322 (A.I.A.)

Abstract: Several physics-based models have been utilized in material design for the simulation and prediction of material properties. In this study, several machine-learning (ML) approaches were used to construct a prediction model to analyze the influence of equal-channel angular pressing (ECAP) parameters on the microstructural, corrosion and mechanical behavior of the biodegradable magnesium alloy ZK30. The ML approaches employed were linear regression, the Gaussian process, and support vector regression. For the optimization of the alloy's performance, experiments were conducted on ZK30 billets using different ECAP routes, channel angles, and number of passes. The adopted ML model is an adequate predictive model which agreed with the experimental results. ECAP die angles had an insignificant effect on grain refinement, compared to the route type. ECAP via four passes of route Bc (rotating the sample 90° on its longitudinal axis after each pass in the same direction) was the most effective condition producing homogenous ultrafine grain distribution of 1.92 μm. Processing via 4-Bc and 90° die angle produced the highest hardness (97-HV) coupled with the highest tensile strength (344 MPa). The optimum corrosion rate of 0.140 mils penetration per year (mpy) and the optimum corrosion resistance of 1101 $\Omega \cdot cm^2$ resulted from processing through 1-pass using the 120°-die. Grain refinement resulted in reducing the corrosion rates and increased corrosion resistance, which agreed with the ML findings.

Keywords: machine learning; linear regression; support vector regression; equal channel angular pressing; ultrafine-grained structure; corrosion behavior

1. Introduction

Magnesium (Mg) alloys have attracted a lot of attention because of their excellent qualities of high specific strength and low density, which are ideal for transportation and lightweight structural sectors [1,2]. On the other hand, Mg alloys also have significant potential in biological applications, where they show promise for application as bone implant materials due to their inherent benefits over typical biomedical materials [3–5].

This is because Mg alloys have superior mechanical properties, are biocompatible, are extremely biodegradable [6–8], and have remarkably similar density and elastic modulus to genuine bone [9]. The high biodegradability of Mg alloys in the human body is one of the most appealing properties of a substance utilized in medicine, as they can dissolve in the body's fluids after surgery, and therefore they do not have to be taken out with another surgery [10,11]. Mg is also very biocompatible and non-toxic, which may help the new bone cells grow and adhere together [12,13].

However, Mg alloys have not been used as much in medical applications because they corrode quickly in systems rich in chloride, and degrade quickly [14] due to the loss of mechanical integrity of bones before they are fully healed. Moreover, the formation of a hydrogen layer in the corrosion-prone areas affects the biodegradability of Mg alloys [15–17]. Consequently, several techniques based on different alloy designs and surface changes have been proposed to enhance the resistance to corrosion (biodegradability rates) and mechanical behavior of Mg alloys [15,18–23]. Other methods, such as eliminating impurities and regulating their content ratios, have also been used to control the degradation rate [24,25]. Accordingly, to facilitate the use of Mg alloys in biomedical applications while maintaining nontoxicity, durability, biocompatibility, and cytocompatibility throughout the service lifespan, it is essential to enhance their rate of corrosion and their mechanical properties [19,26–29].

Numerous investigations have been carried out to find suitable alloying elements to enhance the mechanical and corrosion behavior of magnesium alloys. Aluminum (Al) additions were proven to be a cause of Alzheimer's, hence it was stated that Al might be hazardous and toxic [30]. Similar findings were made regarding liver toxicity caused by other rare-earth elements, including yttrium [6,31]. As a result, it is advised to utilize an Al-free Mg alloy while working with people [32]. However, zinc (Zn) additions offered the chance to improve deformability and ductility. Zn is also a crucial nutrient for the body, and its ions may be easily digested without endangering important organs. Similarly, Zirconium (Zr) has also been described as a biocompatible alloying element when present in low amounts [5,28,29,33]. It was also demonstrated by Gu et al. that Mg alloys with the addition of Zr and Zn were stronger, more resistant to corrosion, and more cytocompatible than pure Mg [32].

Concerning its manufacture, grain refining is a useful technique for enhancing Mg alloys' mechanical properties [19,28,29,34,35]. It is utilized to enhance the uniform corrosion behavior promised by the homogeneous nanoscale dispersion. Hence, grain refinement via severe plastic deformation (SPD) might achieve such properties [36–47]. In addition, it was shown that the reference alloys with the coarsest grains had the most positive pitting potentials [48], while the ultra-fine-grained (UFG) Mg alloys were linked to an amelioration in corrosion resistance. The Mg-Zn-Zr alloy family (ZKxx), which stands to represent a plausible alternative for metallic biodegradable materials, may thus be a better solution for medical implants [19,28,29,49].

ECAP is one of the most significant SPD techniques for refining the grains of metallic materials, which results in enhancing both mechanical and electrochemical behavior [35,50–53]. The ECAP method compels the material to move on a die featuring two parallel channels with similar cross-sectional profiles, and which intersect at a point that has an inner channel angle that is given a symbol of ϕ, and Ψ for its curvature angle [28,29]. The type of ECAP route, and how many passes are needed for the billets that have been processed, both have massive implications for the changes to its mechanical features, the nature of its texture regarding crystallography, and the evolution of its microstructure [54]. The three pervasive types of ECAP route are A, Bc, and C (Figure 1) [28,54]. In route A, the billet goes through several passes with no turning, while route Bc involves a 90° turn after each pass in the same direction across its longitudinal axis [28,46,54], whereas in route C it is turned 180° after each pass across the extrusion direction [54,55].
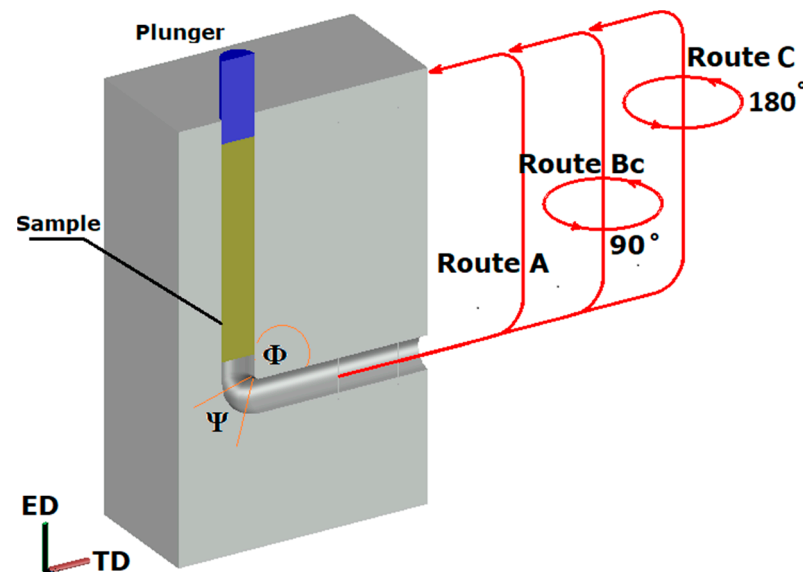
Figure 1. ECAP die showing the processing route types.

Several studies have been carried out to identify how SPD approaches like ECAP affect the way Mg alloys corrode, and particularly to understand the reason that the UFG structure obtained from ECAP makes corrosion resistance better. Grain refining using ECAP reportedly enhanced corrosion performance in ZKxx alloys by creating quite a consistent and even distribution of the added alloying elements [14,56]. One-pass ECAP processing with a custom-made ECAP die of ZK60 has been shown by Orlov et al. [14] to improve corrosion resistance by refining and redistributing the grains of Zn and Zr. Several research works have been directed at investigating the performance of biodegradable Mg alloys in modeled bodily fluids, including Mg-Zn-Zr [28,29,57], AZ31 [34,58], ZK60 [59], and ZN20 [60]. According to Alawad et al. [57], processing the Mg-Zn-Zr alloy at four passes of route Bc utilizing ECAP resulted in a remarkable reduction in the size of grains by around 92.7%, which led to an amelioration in the rate of corrosion by ninety-four percent, in comparison to the as-annealed (AA) equivalents. The corrosion rate was improved by 78.3%, and the Vickers microhardness was improved by 132%, when AZ31 was processed using a 2-Bc ECAP die with a 90° inner channel angle, as reported by Alateyah et al. [34]. According to Mostaed et al. [59], ZK60's corrosion rate and ductility were greatly enhanced after eight passes of processing by route Bc, with a deterioration in mechanical properties. Analysis of ECAP processing's impact on AZ31's stress corrosion cracking was conducted by Peron et al. [58]. As a result of four ECAP processing steps, Gao et al. [60] pointed out an obvious amelioration of 40% in the ductility of Mg-Zn-Nd alloy, along with grain refinement, texture deterioration, and improved corrosion resistance.

The development of diverse material-design approaches, such as the design of experiment methodologies, optimization processes, and physics-based models, has received a great deal of attention amid efforts to investigate and generate innovative materials with distinct properties [61–63]. These traditional approaches frequently require a rigorous physics-based investigation of the relationships between complicated material properties and design concepts. It is consequently vital to analyze and study various fundamental physical and chemical rules that regulate material behavior. Machine learning (ML) models are another novel option that has been put forward as a potential material-design approach. ML is a subset of artificial intelligence (AI) that enables computer programs to accurately predict new outcomes from previously trained data, without explicit programming. These models just need a database to record the complicated interactions between material properties as inputs, and material responses or attributes as the intended models' outputs. The relationships of material attributes are discovered by machine learning models much faster than by using any other traditional approaches for material design, and with a high degree

of accuracy. Due to the recent rapid expansion in computer performance and capabilities, as well as the accessibility of enormous datasets and fully deployed sophisticated algorithms, the ML field has seen a surge in attention for several industrial purposes. ML techniques are presently being used effectively to tackle massive datasets with high-dimensional inputs comprising regression, classification, clustering, and dimensionality reduction. The use of ML technology helps quickly manage and expose complex material systems (including their sudden functional changes), extract knowledge from the given data, and predict the properties of the system. Furthermore, by adding extra data to ML models, it is possible to use them as a tool for data analysis, producing forecasted results regardless of the model that was chosen [64,65].

The aforementioned literature shed light on the possible biomedical applications of Mg alloys and, as a result, the promising industrial applications that will develop from enhancing their degradation and mechanical behavior. Thus, the aim of this paper is two-fold. First, to investigate the corrosion behavior of ECAP-processed ZK30 alloys in simulated body fluids. Second, to analyze and optimize ECAP processing parameters to improve the ZK30 alloy's corrosion performance and mechanical properties. To that end, in the current research, investigations were carried out to ascertain the effect of the ECAP processing on the corrosion rates, mechanical behavior, texture, and structural evolution of the ZK30 alloy. Variable ECAP routes and multiple passes were investigated. Machine learning methods and approaches were used here to develop a predictive model for the ZK30 alloys processed via ECAP. Linear regression (LR), Gaussian process regression (GPR), and support vector machine (SVM) for regression (SVR) were among the ML algorithms adopted for model training and validation. Several assessment criteria, including residuals (r), mean squared errors (MSE), root mean square error (RMSE), and coefficient of determination (R^2-score), were used to validate and analyze the trained models.

2. Methodology

2.1. Material and Experimental Procedure

In this investigation, a commercial ZK30 alloy (Mg-3Zn-0.6 Zr, wt%) was adopted. ZK30 billets 20 mm in diameter and 60 mm in length underwent a 16-h annealing process at 430 °C. The adopted dies for the ECAP used two crossing cylindrical channels with an external angle of $\Psi = 20°$ and internal angles of $\Phi = 90°$ and $120°$ to be performed on the AA samples of the billets as shown in Figure 1. One pass (1P), two passes (2P), and four passes (4P) of the ECAP process were performed while placing the temperature at 250 °C, employing a speed of the ram set at 10 mm/min, at different deformation settings, and using routes A, Bc, and C.

The microstructural and textural development of the ZK30 alloy was researched by adopting a cross-sectional cut taken longitudinally from the midpoint of the material using ground and polished samples. For the polishing process, diamond suspensions were used containing particles of 3 μm, subsequently 1 μm, along with a yellow DP-lubricant (mixture of 90% ethanol +10% isopropyl alcohol). In order to achieve this, the last polishing procedure was performed using a 0.05-micron colloidal silica formula. The following stage involved etching the samples for 50 s in a solution of 5 milliliters of acetic acid (95%), 10 milliliters of water, 100 milliliters of ethanol, and 6 g of picric acid. Lastly, the resulting samples were then flat ion milled utilizing a flat ion milling system for 30 min to eliminate the top amorphous layer. The milling settings were set at a 5° grazing angle, 0.425 s^{-1} specimen rotation speed, and 2 keV beam energy [28,29]. Ion milling was employed for sample preparation for subsequent texture analysis.

An SU-70 SEM outfitted with an electron backscatter diffraction (EBSD) attachment was utilized to evaluate the advancement in the ZK30 biodegradable alloy's microstructure and the progression in the anticipated crystallographic texture. The ECAP-processed billets were sectioned down the center longitudinally, parallel to the pressing direction, to produce samples for SEM and EBSD analysis. The reference system's axes align with the extrusion ECAP direction (ED). The EBSD data were collected from the top surface ED

plan in increments of 100 nm adopting the HKL Flamenco Channel 5 software (Hitachi, Ltd., Tokyo, Japan), where the SEM was functioning at a current of 1.5 nA and a voltage of 15 kV [28,29]. The contouring parameters were based on more than 10-pixel, data clustering of 5 degrees and half-width of 10 degrees.

The corrosion performance of the ECAP-processed ZK30-Mg alloy was assessed utilizing a three-electrode corrosion cell. Rectangular samples measuring 20 mm by 30 mm were cleaned with acetone and then ground using silicon-carbide sheets up to 4000 grit. One ZK30 sample that had been ECAP-processed served as the working electrode, while a saturated calomel electrode (SCE) and a platinum mesh served as the reference and counter electrodes, respectively. Ringer lactate corrosive agents were examined for corrosion at room temperature. Adopting a Luggin capillary increased measurement accuracy and decreased ohmic drop. The readings were taken and recorded employing an SP-200 Potentiostat, where the steady-state condition was further verified using the polarization approach at a prospective rate of scanning at 0.2 mVs^{-1}. Linear potentiodynamic polarization was performed using an open circuit voltage with a prospective voltage ranging around ± 250 mV. Electrochemical impedance spectroscopy (EIS) was employed at open-circuit potential (Ecorr), with a sinusoidal voltage of 10 mV and a frequency range of 10 MHz to 100 kHz.

Mechanical behavior characterization was carried out before and after the ECAP passes. Vicker's microhardness examination (HV) was performed utilizing a digital microhardness tester (Qualitest Canada Ltd., Nisku, AB, Canada), from the sample periphery to the middle of the processed samples, at 0.5 kg load and 15 s dwell time. The average results were calculated over a minimum of five equally spaced indents per site. Tensile properties were characterized at room temperature and a strain rate of 10^{-3} s^{-1}, using a 100 kN universal testing machine (Instron 4210, Norwood, MA, USA). The adopted samples for the tensile tests were selected from the middle of the ZK30 ECAP-processed samples and machined to E8M/ASTM tensile sample dimensions. Three samples were tensile tested per processing condition compared to the as-received one.

2.2. Machine Learning Approach

The probable processing route type, the estimated number of passes needed, and the adopted die angle of the ECAP were the most commonly reported ECAP process parameters in previous findings [53]. According to earlier research [28,29], 16 runs were conducted to test various ECAP responses. The specific levels of the adopted ECAP process parameters used in this analysis, and the experimental design, are presented in Tables 1 and 2, respectively. These parameters included the number of passes needed, which are presented as 1, 2, or 4, the adopted die angles of the ECAP, which were set at 90° and 120°, and the chosen processing route types, from A, Bc, and C.

Table 1. The ECAP process parameters and their subsequent levels.

ECAP Parameters	Process Parameters Levels		
	−1	**0**	**1**
Number of passes	1	2	4
ECAP die angle	90	120	-
Processing route type	A	Bc	C

Supervised learning, unsupervised learning, semi-supervised learning, and reinforcement learning are the major important fields within ML. The most common kind of ML is supervised learning, which examines training data with the goal of identifying patterns and making predictions based on past data [66]. Data preprocessing, model initialization, feature extraction from input data, active learning algorithm selection, model training, validation, and testing are all part of the unsupervised learning framework. Supervised and unsupervised learning frameworks are the most widely adopted techniques [66]. In the unsupervised learning framework, the training dataset is used to learn, and it provides

a good match for the model parameters. The majority of the methods adopted for mining training data for the purpose of reaching empirical correlations are data-suitable in the way they reveal existing relationships that were overlooked in the data in the first place. Model variables are fine-tuned by using a validation dataset. Both the training dataset and the validation dataset should have the same probability distribution. An independent testing dataset with the same probability distribution as the training dataset is adopted to evaluate the model. The next step in the training process involves optimizing the model's performance, which is often measured by a cost function. The training procedure, model structure, and behavior are all often affected by hyperparameters that must be modified throughout this process. In a perfect world, the hyperparameters would be improved with data that was not used in the test or training. During model training, an overfitting problem can arise when a model overfits the dataset to a perfect match without taking the regularization rule into account. In such a scenario, the trained model nearly never does well during validation in the testing phase. With a small dataset like the one in this study, cross-validation (CV) is employed to ensure that the model is not overfitting. The training data is partitioned into many small, independent subsets called "folds" using the k-fold CV method. Each k-fold of data is adopted to train the model, which is then tested by utilizing the remaining data as a test set aimed at seeing how well it performs. This procedure is redone k times in a loop. The effectiveness of the model is measured by calculating the average of the iteration's data values. While this approach is computationally expensive, it does help conserve data, particularly if the model has been trained using a limited dataset.

Table 2. The experimental design of the ECAP process parameters.

Run	A: No. of Passes	B: Die Angle	C: Route Type
AA	-	-	-
1	1	120	Bc
2	2	120	A
3	4	90	C
4	2	120	C
5	2	90	Bc
6	2	120	A
7	2	90	Bc
8	4	120	Bc
9	4	120	C
10	2	120	Bc
11	1	120	C
12	4	90	Bc
13	1	90	A
14	4	90	A
15	4	90	A
16	1	90	C

An effective predictive ML model was developed using Gaussian process regression (GPR) and support vector machine (SVM) for regression (SVR) to forecast the ECAP parameters of ZK30 alloys. Brief descriptions of the methods used will be provided below.

2.2.1. Gaussian Process Regression (GPR)

Recent advances in ML have been made possible in part by the GPR methodology, which falls into the category of Bayesian regression techniques for nonparametric data [67]. The technique presents several benefits, including the capacity to excel on tiny datasets and produce estimations of prediction uncertainty. Recently, the GPR methodology has received much interest and has been applied to various research topics, especially in chemistry and materials science [68].

Taking into account the training dataset (x_i, y_i); i = 1, 2, ... , M, where $x_i \in \mathbb{R}^d$ and $y_i \in \mathbb{R}$ are taken from an unidentified distribution, and M is the number of observations or instances in the dataset. The new input vector x, along with the training data, is designed

to estimate the outcome of a response variable y utilizing a GPR model. The structure of a linear regression model is as follows:

$$y = x^T \beta + \varepsilon \tag{1}$$

where the error term is $\varepsilon \sim N (0, \sigma^2)$, and β vector is the predicted coefficient that best fits the model. N () denotes a normal distribution with a mean of zero and an error variance of σ^2. A Gaussian process (GP) is often characterized by its two famous functions, the mean m(x) and covariance (or kernel) k (x, x′) functions, where x and x′ are two instances of the input features of matrix x. Consequently, a GP could be employed to represent the expected values of y:

$$y^* \sim GP(m(x), k(x, x')) \tag{2}$$

Given that the covariance function plays a crucial role in determining how well GPR performs, it must be carefully selected or built. Although there are several common covariance functions in the GPR, picking one depends on the circumstances of each individual situation. The radial basis function, one of the well-known kernels that are frequently used with GPR, is stated as [67]:

$$K(x_i, x_j) = \exp\left(-\frac{\|x_i - x_j\|^2}{2\sigma^2}\right) \tag{3}$$

where the kernel function's spread is represented by σ and $\|x_i - x_j\|$ is the Euclidean distance between the two feature vectors.

2.2.2. Support Vector Machine (SVM)

When it is necessary to model a problem aimed at classifying data or perform regression problems using ML, the SVM technique [69] is extensively employed. The classification processes used by SVR are similar to those of the SVM with a few minor modifications [70–73]. For regression, a tolerance margin (ε) is provided to the SVM as an approximated estimation that the problem would have already requested; moreover, the algorithm complexity should be carefully considered. The idea of the SVM technique is based on partitioning data into multiple groups with the greatest margin, where the algorithm selects the best hyperplane. $f(x)$ is adopted to provide the best approximation for the supplied training dataset (x_i, y_i), $i = 1, 2, \ldots , M$, where x is a multivariate collection, and M is the number of instances in the dataset. The function $f(x)$ could be presented as follows in its most straightforward way:

$$f(x) = wx + b \tag{4}$$

Minimizing the next formula [68] would lead to the required optimum values of w and b:

$$\text{Min } \frac{1}{2}\|W\|^2 + C \sum_{i=1}^{N}(\xi_i + \xi_i^*) \tag{5}$$

Subject to:

$$\begin{cases} y_i - wx_i - b \leq \varepsilon + \xi_i \\ wx_i + b - y_i \leq \varepsilon + \xi_i^* \\ \xi_i, \ \xi_i^* \geq 0 \end{cases} \tag{6}$$

where ε is an error tolerance termed as the ε-insensitive tube, and the term C is a balance parameter between the error term that is expected empirically and the generic term. Whereas ξ and ξ^* are the slack variables, representing the individual fitting errors for each data point. This allows for errors around the regression function and consequently provides model

regularization. The output of the regression function is then obtained utilizing Lagrangian multipliers and the optimum constraints [69]:

$$y = \sum_{i=1}^{N}(\alpha_i + \alpha_i^*)K(x_i, x) + b \tag{7}$$

where α, α^* are the Lagrangian multipliers, and $K(x_i, x)$ is the kernel function. Among the foremost prominent kernel functions frequently employed with SVR are linear, polynomial, sigmoidal, Gaussian, and radial basis functions.

3. Results and Discussion

3.1. Analysis of Machine Learning Approach

The estimated Pearson's coefficient for every combination of parameters is revealed in the matrix of the input data shown in Figure 2, along with the corresponding correlation chart. Each off-diagonal subplot displays a scatterplot for two parameters, and each diagonal subplot displays a histogram for the given parameter's distribution. In each off-diagonal subplot, the slope of the least-squares reference line equates to the correlation coefficient. Assuming a linear relationship between the two sets of data, the Pearson correlation coefficient $\rho(x,y)$ for this graph could be calculated in the following way:

$$\rho(x,y) = \frac{1}{N-1}\sum_{i=1}^{N}\left(\frac{x_i - \mu_x}{\sigma_x}\right)\left(\frac{y_i - \mu_y}{\sigma_y}\right) \tag{8}$$

where μx, μy and σx, σy are the mean and standard deviation of variables x, and y, respectively. The correlation coefficient is usually between (-1) and (1). Slopes of linear relationships between the two parameters are positive when they are increasing, and negative when they are decreasing. A coefficient value close to positive one indicates a strong directly proportional correlation, whereas a coefficient value close to negative one indicates a strong inversely proportional correlation, while a coefficient value close to zero indicates a weak correlation.

The correlation figure also shows that the hardness (H), yield stress (σy), and tensile strength (σu) are all positively influenced by augmenting the number of passes (N), with substantial positive correlations at 0.76, 0.45, and 0.58, respectively, whereas the elongation (El) and grain size (GS) exhibited a strong negative correlation of -0.57 and -0.75, respectively. These results are corroborated by experimental data showing that the σy and σu values of ECAP-processed billets are significantly higher than those of their AA counterparts. Note that El falls off precipitously as strength intensifies. Moreover, these results agree with the exhibited substantial decrease in grain size that comes with an increase in the number of passes and the corresponding increase in σu, as will be presented in Sections 3.2.1 and 3.2.2, respectively. These findings agree with those of Dumitru et al. [74], who claim that an increase in σu might have been caused by an increase in both the dislocation density and the number of second-phase particles as a result of increasing the number of ECAP passes. Additionally, these outcomes agree with the findings of the microstructural evolution, where the increase in the number of passes led to further refinement, resulting in smaller grain sizes with increased passes. ECAP processing with many passes gradually transforms the LAGBs into HAGBs, which is linked to the development of UFG, which increases the size of the grain boundary and consequently acts as a barrier against dislocation motion, leading to increased alloy hardness and strength.

The results also show that the tensile properties of σy and σu decline when the ECAP die angle (φ) is increased, with negative correlations of -0.63 and -0.65, respectively. On the other hand, the ECAP die angle (φ) has a positive effect on El, with a positive correlation of 0.48. These outcomes were also reinforced by the experimental outcomes, where it was demonstrated that the most substantial enhancement in tensile properties was obtained under processing conditions comprising a 90° ECAP die angle, pointing at the

lower utilized angle, which could be assigned to the increased plastic strain. Moreover, an improved El was seen at route Bc with a 120° die angle and four passes in comparison to route Bc with a 90° die angle and four passes, which agrees with the obtained correlation plot outcomes.
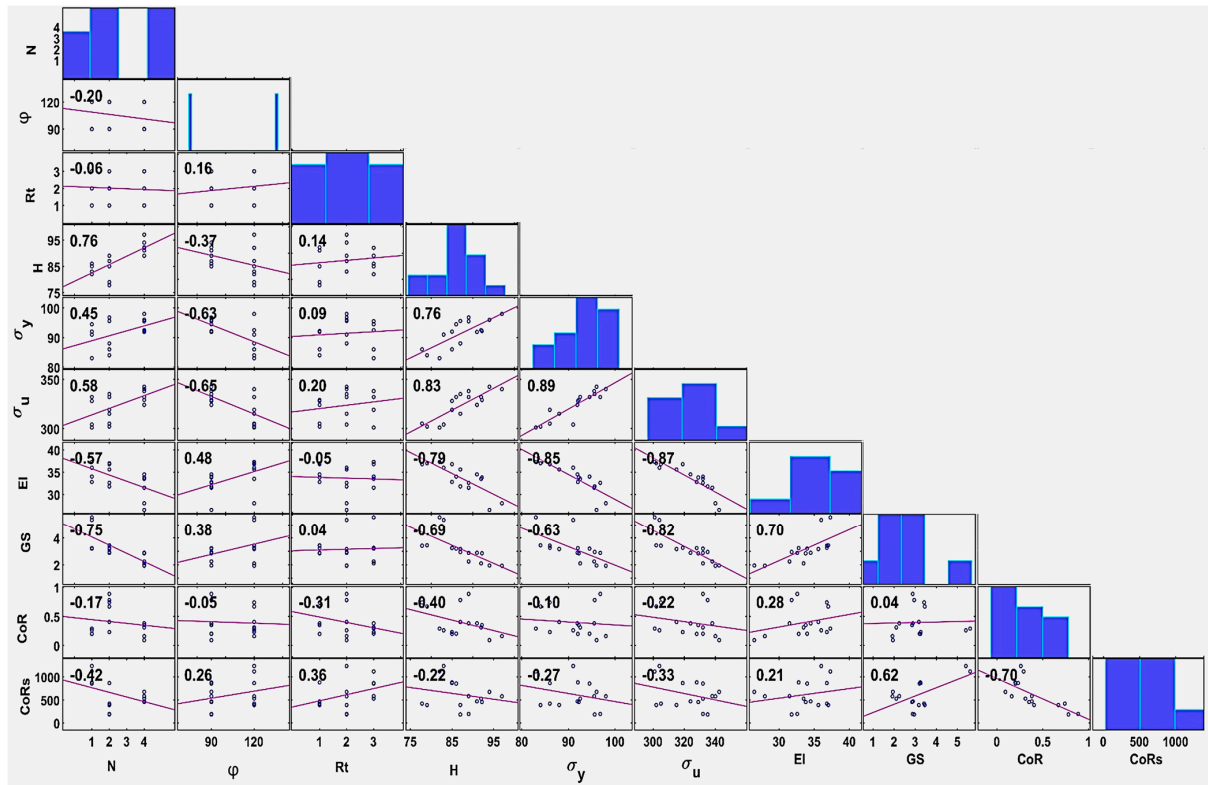

Figure 2. Correlation chart of Pearson coefficient linear regression plots of every two pairs of properties responding to ECAP parameters hardness (H), yield stress (σy), tensile strength (σu), elongation (El), grain size (GS), corrosion rate (CoR), and corrosion resistance (CoRs) against alloy feature parameters number of passes (N), die angle (φ), and route type (Rt). A coefficient value close to one suggests a strong correlation between two variables, whereas value close to zero indicates a weak correlation. Positive slopes indicate positive correlations, whereas negative slopes specify negative correlations.

3.2. Effect of ECAP Processing Parameters

3.2.1. Microstructural Evaluation

The grain structure of the ZK30 was evaluated using EBSD, and all of the AA-ZK30 orientation maps in Figure 3 are shown in relation to the extrusion direction (ED). Moreover, experimental findings for the average grain size of AA and ECAP-processed ZK30 alloy billets are shown in Table 3. Figure 3a shows the AA-ZK30 orientation map, which depicts areas with fine grains and with spaced coarse grains. Figure 3b,f show the microstructure of the AA-ZK30 processed using 1P ECAP via die angles of 90° and 120°, respectively. Processing at 1P via 90° intersecting ECAP channels resulted in scattered zones with ultrafine grain surrounding coarse grains, which is indicative of nonuniform strain distribution while passing through the shear zone. Conversely, 1P via 120° intersecting channels revealed lower grain refinement, yet with a higher degree of uniformity that is indicative of lower effective strain. Augmenting the number of passes enhanced the structure uniformity as evidenced by the disappearance of the scattered coarse grains compared to 1P processing. Further grain refinement was observed when increasing the number of passes to four via routes A (Figure 3c), Bc (Figure 3d), and C (Figure 3f). Figure 3d shows that route Bc produced finer grain sizes with a higher degree of uniformity compared to routes A and

C. In addition, it is obvious from an examination of Figure 3d that processing 4-Bc passes using the 90°-die results in increased regions of ultrafine grain structure (UFG), in spite of the existence of comparatively coarse grains. The average grain size measured was the finest for the 4-Bc processed billets using a 90° die angle compared to the 4-A and 4-C ones, as listed in Table 3. Based on the measured grain size and their corresponding average and standard deviation, it is clear that the average grain size was not significantly influenced by ECAP processing angles of 90° and 120° (Table 3). This was demonstrated by the fact that processing via 4-Bc with the 90°-die and 120°-die decreased grain size by 92.7% and 92.8%, respectively, compared to their AA counterparts. However, the standard deviation revealed a much higher value for the 90° angle compared to the 120°, which is indicative of a wider grain size distribution around the mean value. This is indicative of the enhanced grain size uniformity via the 120° ECAP die compared to the 90° one.

Table 3. The data of grain size for the AA and ECAPed Mg-Zn-Zr billets. All of the presented units are in μm.

	AA	90°-Die				120°-Die	
		1P	4A	4Bc	4C	1P	4Bc
Minimum	3.39	1.13	0.23	0.23	0.28	2.24	0.76
Maximum	76.73	38.10	14.53	11.76	12.73	35.22	17.86
Average	26.69	3.24	2.89	1.94	2.25	5.43	1.92
St. Deviation	14.74	2.42	1.92	1.54	1.60	4.22	1.09

The experimental results in Figure 3 and Table 3 revealed an agreement with the reported results by other researchers [28,29,56,74] concerning the density of low-angle grain boundaries (LAGBs). The current structural analysis revealed a significant increase in the LAGB structure following the first pass, which decreased as the number of processing passes increased [75]. Dislocation density increased during the first pass, creating LAGB dislocation cells [76]. The larger proportion of high-angle grain boundaries (HAGBs) associated with ECAP 4-Bc condition, as opposed to the 1P counterpart, demonstrates that the LAGBs underwent recrystallization over successive passes, resulting in the evolution of LAGB dislocation cells into grains with higher misorientation angles. Here, it is important to note that the completion of the dynamic recrystallization (DRX) process is manifested by the change of LAGBs into HAGBs [75], which strengthens the alloy by impeding and blocking the dislocations' movement [77]. Similar results were found in a previous investigation [60]. Microstructural changes that occur during the ECAP processing of Mg alloys have been modeled in detail by Figueiredo et al. [78]; they showed that the microstructure of Mg alloys changes from a monomodal distribution to a bimodal or multimodal distribution in the first pass and that successive passes substantially improve the microstructure. In conclusion, a UFG homogenous distribution microstructure ought to be acquired when a sufficient number of passes have been completed.
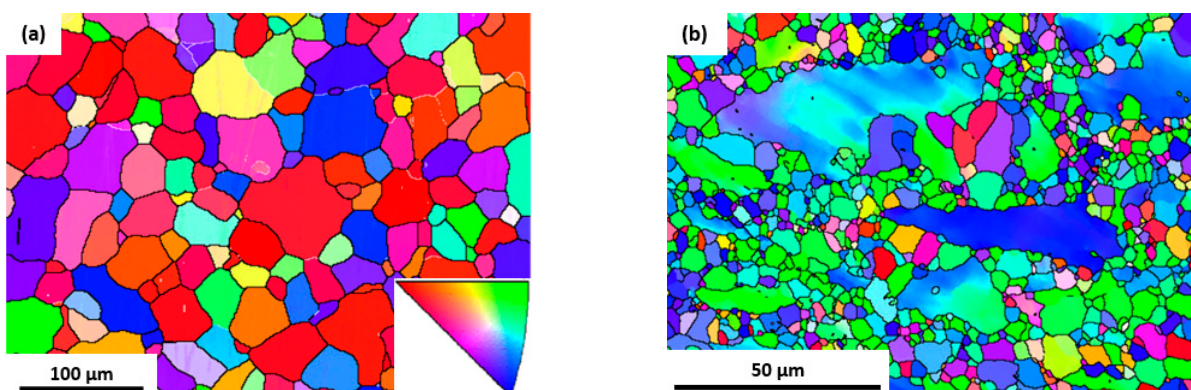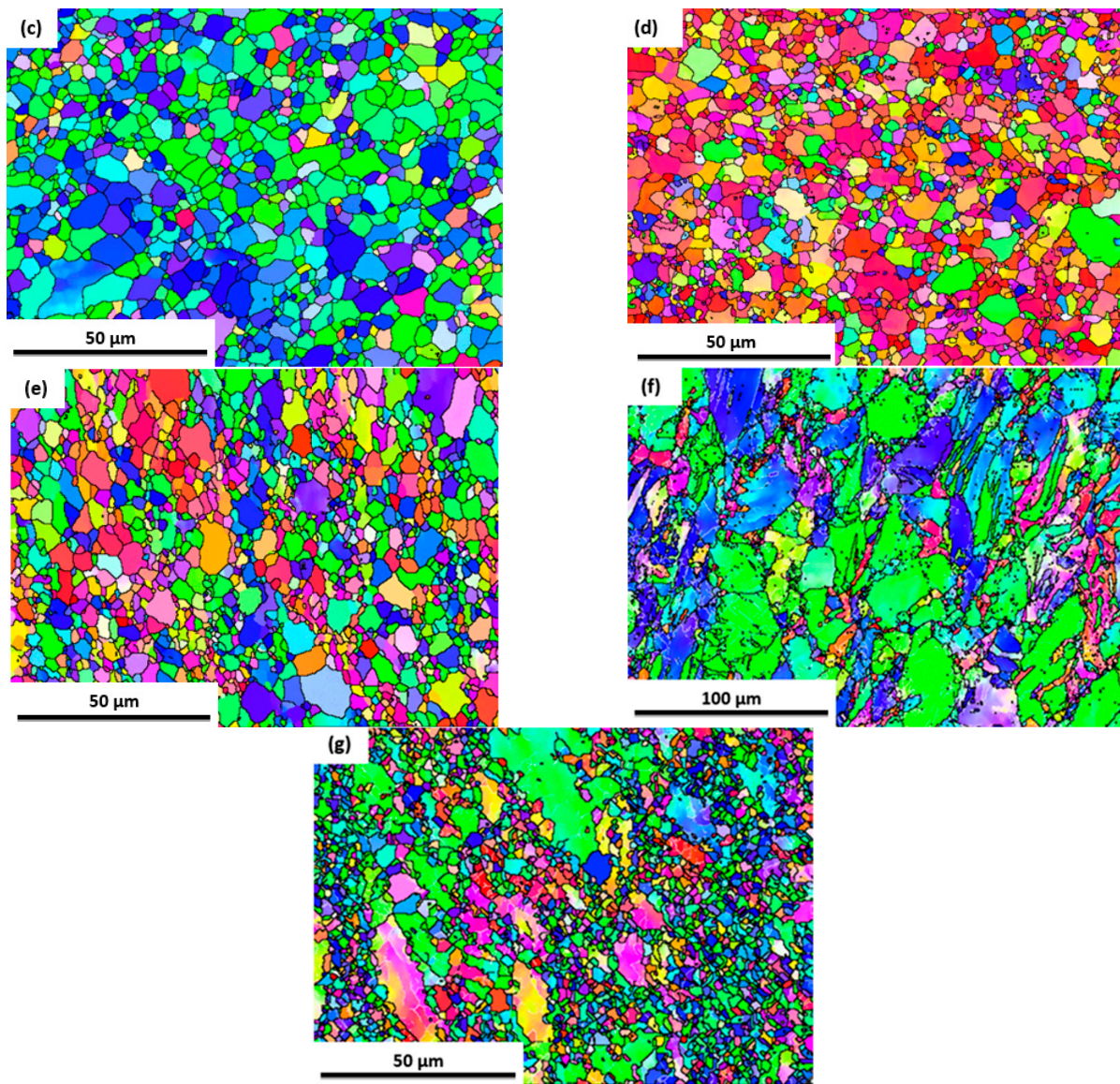

Figure 3. *Cont.*

Figure 3. EBSD orientation maps for the AA-ZK30 (**a**) and post-ECAP processing over 1-P (**b**), 4-A (**c**), 4-Bc (**d**), 4-C (**e**) using the 90° die angle, and 1P (**f**), 4-Bc (**g**) by the 120°-die angle. The inverse pole figure (IPF) coloring triangle is depicted in for the 90°-die and 120°-die, red: [001]; blue: [120]; and green: [010].

The {0001} pole figures of the AA condition are exposed in Figure 4a, whereas 1P, 4-Bc, 4-A, and 4-C (90° die angle), and 1P, 4-Bc (120° die angle) ECAP processed ZK30 billets are shown in Figures 4b–e and 4f,g, respectively. The AA texture (Figure 4a) has a highest texture intensity of 14.3 times random, and it is characterized by a strong {0001} <uvtw> fiber texture with intense {0001} poles that are positioned at an angle with respect to the extrusion direction (ED). In accordance with [35], the crystallographic texture that developed during ECAP processing was primarily the simple shear texture with the shear plane oriented at 45° relative to the extrusion direction. There are three levels of slip systems in HCP crystal structures (Mg alloys): basal {0001} <11–20>, prismatic {10–10} <11–20>, and pyramidal {10–11} <11–20> [86,87]. Robust basal plane texture components with a highest texture intensity of 20.8 times random were produced by ECAP via 1P processing for the 90°-die, as shown in Figure 4b. With the 1P condition, the {0001} basal planes were twisted roughly 30° with respect to the ED. By turning the ECAP-processed billet on its central longitudinal axis while processing at 4-Bc, the {0001} basal planes were twisted roughly

45° with respect to the ED, resulting in a different crystallographic texture (Figure 4c). The highest texture intensity was reduced to 8.46 times random after being processed with 4-Bc because there are only so many ZK30 slip systems available during shear deformation [79]. As a result of 4-A processing, ZK30 billets have {0001} basal planes that are 45° off of the ED. Processing in 4-A resulted in a highest texture intensity that was equal to 8.77 times random. Figure 4e demonstrates that after going through ECAP processing in 4-C, the highest texture intensity was augmented to 9.51 times random, and the {0001} basal planes were slanted nearly 45° apart from the ED. Several of the {0001} basal planes in the 120° ECAP die were positioned parallel to the transverse direction (TD) after being processed in 1P, while the other {0001} planes were turns on the TD axis by about 45°, which could be explained as the c-axes are 45° off of the ED and coplanar to the shear plane normal (SPN), as depicted in Figure 4f; moreover, two overlapping peaks on the {0001} pole figure could be observed.
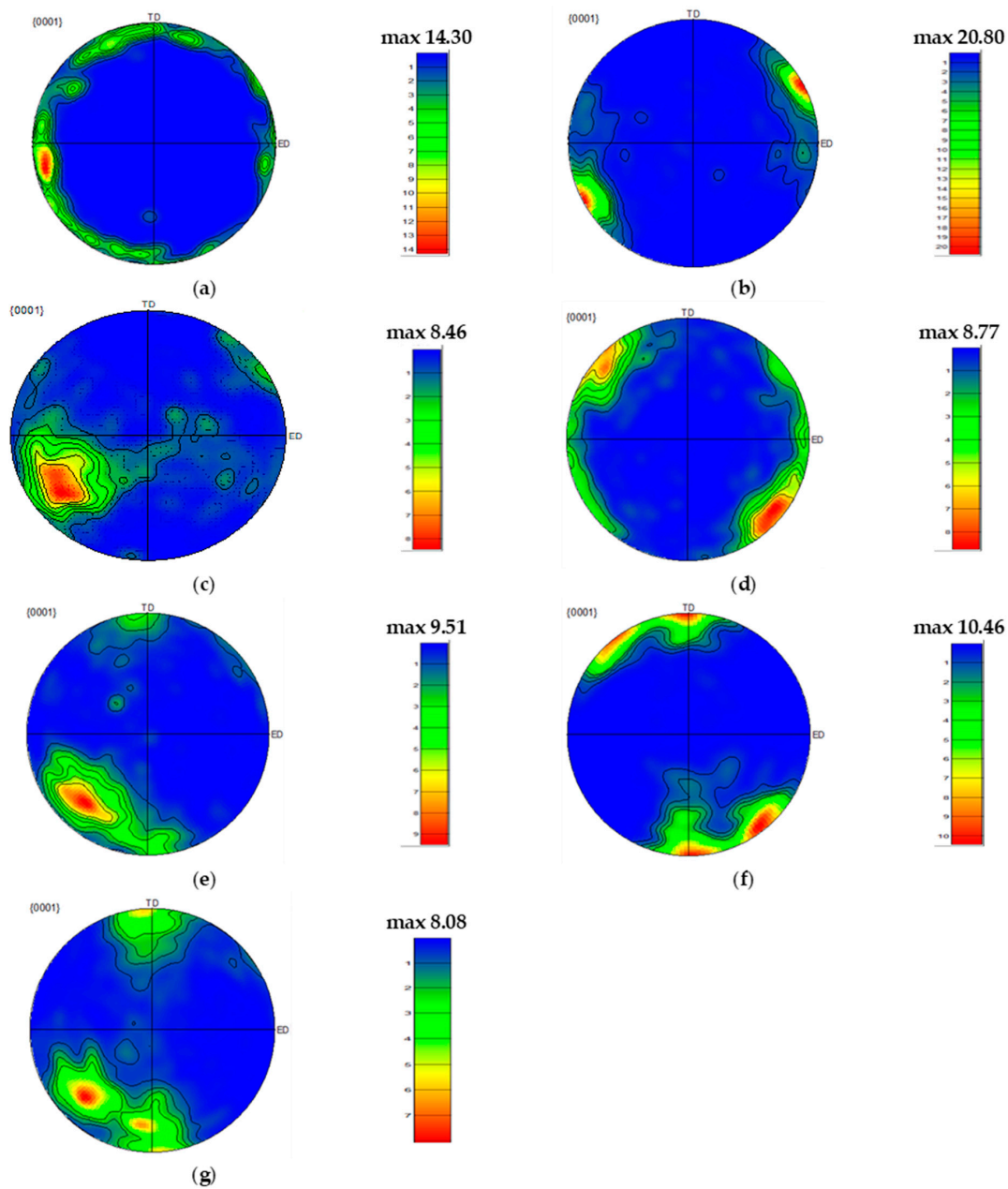

Figure 4. {0001} pole figures showing the crystallographic texture of the AA billets (**a**) and post-ECAP processing by 1P (**b**), 4-A (**c**), 4-Bc (**d**), 4-C (**e**) with the 90°-die and 1P (**f**), 4-Bc (**g**) with the 120°-die.

From Figure 4 it is clear that the highest texture intensity went down from 14.3 times random (AA billets) to 10.46 times random. Especially remarkable is the fact that the texture's symmetry was almost entirely lost after 4-Bc, along with a corresponding decrease in intensity to 8.08 times random.

Earlier investigations also revealed alike results. Referring to Suh et al. [80], the texture component intensity of the AZ31 alloy was found to be modestly enhanced by using route Bc as opposed to the various other routes. Additionally, they discovered that the novel texture component created after initial passes was reinforced, and the tendency of the Mg alloy's basal planes to align parallel with the rolling direction was enhanced by following route A. Furthermore, they stated that texture intensity was considerably reduced with each even pass along route C, rather than being restored. Since route C leads to a shear stress on the very same plane only in opposing directions every couple of passes, the texture intensity was found to decrease after 4-C processing. Shearing stresses parallel to the basal planes, which occur during ECAP processing, are responsible for the rotation of the basal planes [81]. It was affirmed using XRD that the vast majority of basal poles are rotated by around 45° with respect to ED and TD [82]. The results of the crystallographic texture analysis agreed with those of [83] for the AZ31B Mg alloy, ref. [75] for the Mg-Zn-Ca alloy, ref. [84] for the pure Mg, ref. [85] for the AM60 Mg alloy, and ref. [86] for the Mg-5.00Zn-0.92Y-0.16Zr alloy.

The ECAP properties of the ZK30 alloy were modeled using several ML approaches, including linear regression (LR), Gaussian process regression (GPR), and support vector regression (SVR). After training, the model's performance was evaluated using RMSE and R^2-score. As listed in Table 4, the LR modeling failed to adequately fit the model data, while the SVR was able to model the dataset to some extent. The best-fit model was attained using the GPR algorithm with RMSE and R^2 values in the training set of 0.0176 and 0.99, respectively; in the testing set, these evaluation metrics were 0.3285 and 0.70, respectively. According to Figure 5a,b, the expected grain size values were in strong agreement with the empirical data in both the training and testing datasets. Following successful training, validation, and testing of the ML model of choice, a common strategy is to use the entire dataset to reevaluate the model accuracy and build a more regularized final model appropriate for deployment. From the ML model, it was clear that the number of passes was the most effective processing parameter to determine the average grain size of the ZK 30 alloy, as it exhibited a strong negative correlation of −0.75 (Figure 2). Furthermore, the ML model confirmed that ECAP die angle had a significant influence on the average grain size, with a positive correlation of 0.38. On the other hand, the route type showed a trivial effect on the average grain size compared to the other processing parameters as displayed in Figure 2. The ML model showed that the optimum processing parameters for the magnesium alloy were 4-Bc adopting the 120° channel angle die which exhibited a mean grain size of 1.86 μm. For the 90°-die, the minimum average grain size produced through 4-Bc was 1.88 μm.

Table 4. Model evaluation metrics of ZK30 alloy grain size.

Algorithm	Training Set		Testing Set	
	RMSE (μm)	R^2	RMSE (μm)	R^2
LR	0.6693	0.60	0.5725	0.07
SVR	0.0181	0.99	0.3703	0.61
GPR	0.0176	0.99	0.3285	0.70

3.2.2. Corrosion Behavior

Electrochemical testing studies were conducted on the AA and the biodegradable ZK30, which went through ECAP at varying processing parameters, as described in [28,29], where the observations were performed in an electrolytic solution of ringer's lactate, which is a representative of bodily fluids, to ensure accuracy. Both the potentiodynamic

polarization curves (a) and Nyquist plots (b) of the ZK30 for varying values of the ECAP parameters are shown in Figure 6.
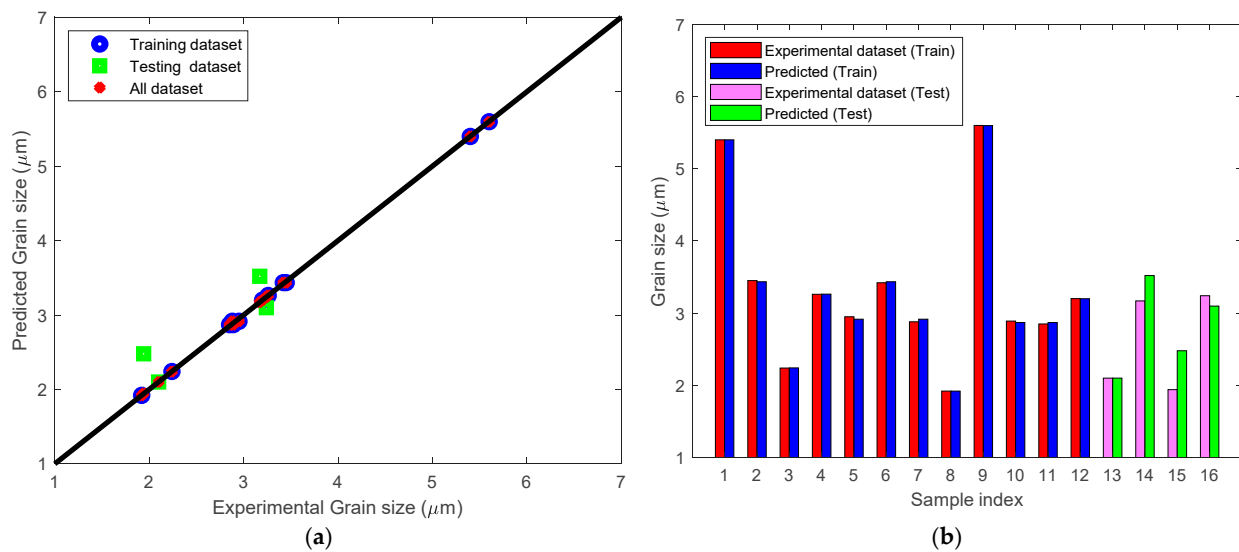

Figure 5. (**a**) Predicted grain size against measured grain size assessed for the training and the testing datasets, (**b**) Predicted grain size against sample indices for predicted training, testing, and experimental dataset.

The Tafel plot is an extremely effective tool adopted for corrosion resistance [87]. Figure 6a demonstrates that the corrosion possibility of 1P using the 90°-die scenario was significantly lower than that of its AA equivalent and that the noble corrosion current shifted noticeably toward the lesser current density (Icorr). With the exception of the 90° 4-C route, further ECAP processing passes, namely those employing the 90°-die and occurring along other routes, led to an additional reduction in corrosion current relative to the 1P pass. Corrosion Icorr was also drastically reduced by raising the die angle to 120° by route Bc, as compared to 90°_4-Bc. It should be noted that when the Icorr value goes down, that may be a good sign that the corrosion rate has been slowed. A change to greater negative values for the corrosion potential Ecorr was seen when the die angle was increased to 120° at 4-Bc.

Nyquist plots showed that the results of the EIS were equivalent, though the diameters of the semicircles were not. The charge resistance, and hence the corrosion rate, are strongly related to the diameter of the semicircle. Therefore, the highest corrosion resistance is found in semicircles with the biggest diameters [52]. Figure 6b demonstrates that in contrast to the ECAP-processed billets, the AA-ZK30 reaction produced the narrowest semicircle. Additionally, the semicircle diameter increased dramatically during 1P ECAP processing with the 90°-die. Nonetheless, the semicircle diameter increased from 1P after four passes of ECAP processing, possibly because strain accumulation boosts dislocation density [28,52,88]. In contrast, as depicted in Figure 6b, the various routes have a major effect on corrosion resistance. The smallest semicircle diameter was achieved via Route C. Nevertheless, the semicircle diameter for Route A is just slightly larger than that for Route 4-Bc. Concerning the effect of the die angle, Figure 6b revealed that processing by 1P with the adoption of a 120°-die resulted in a much greater semicircle diameter in contrast to samples obtained from 1P with the adoption of a 90°-die, which could be interpreted to mean that the augmentation in the imposed strain caused a decline in the corrosion resistance. Moreover, the semicircle diameter rose when employing the 120° ECAP dies in 4-Bc, as opposed to the 90°-die used in 4-Bc, indicating greater corrosion resistance. Increased plastic strain during ECAP processing at 90°-die results in a higher density of dislocations, which reduces corrosion resistance compared to a 120°-die, as previously

documented in the literature [34,58]. To that end, an increase in dislocation density brought about a decline in corrosion resistance.
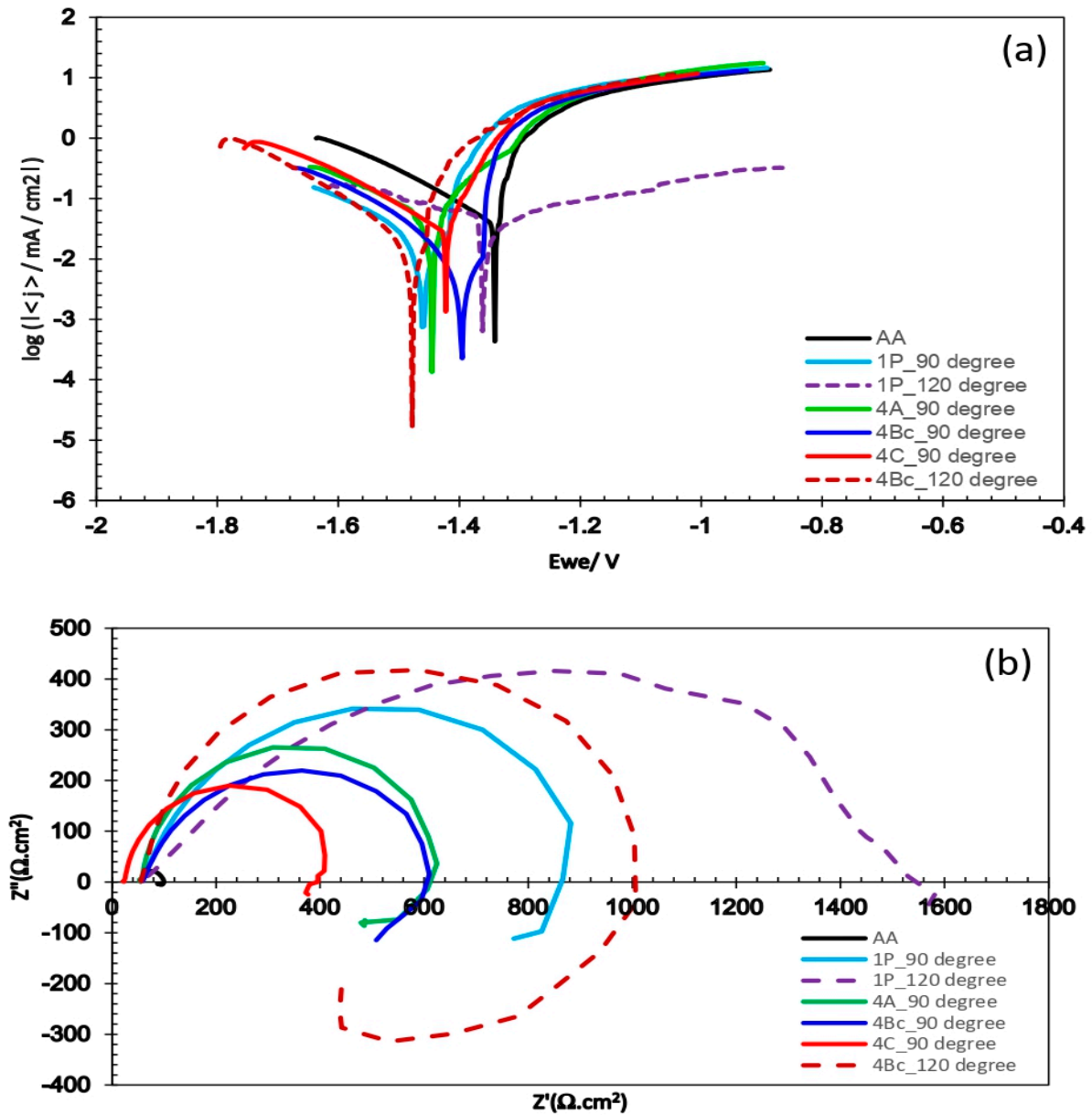

Figure 6. Corrosion outcome readings (**a**) potentiodynamic polarization curves, and (**b**) Nyquist plot for the AA condition and the billets that went through ECAP with varying parameters.

The ECAP-processing-induced improvement in corrosion resistance was linked by Peron et al. [58] to the ameliorated stabilization of the accompanying oxide layer, which revealed small grains. It has been found [19,34] that raising the SPD by augmenting the passes ameliorates the protective layer thickness. Thus, the ECAP-processed ZK30 alloy's corrosion behavior improved due to the formation of high-potential phases, which was enabled by the second phase strengthening mechanism [34], which was in line with the results of other studies. According to Tang. et al. [89], processing the AM80 alloy with ECAP prompted the second phase $Mg_{17}Al_{12}$ to precipitate from the α-Mg matrix, which was responsible for the remarkable augmentation in the ultimate intensity of the β-$Mg_{17}Al_{12}$ phase. As shown by Cubides et al. [90], augmenting the ECAP passes produced more homogenous shielding layers of oxide, which improves resistance to the concen-

trated breakdown of the destructive groups by preventing the involvement of anodic and cathodic sites.

This study's potentiodynamic polarization results and EIS results confirmed that the greatest improvement, resulting in the finest grains, was attained with the 4-Bc, which led to a substantially reduced rate of corrosion to 0.091 mpy as opposed to the cases of 4-A and 4-C processed under similar circumstances. Gurao et al. [91] obtained similar results for pure titanium, which is available on the market. They went through three passes of processing with the adoption of routes Bc, A, and C. It was shown that 3-Bc and 3-A had the least Icorr and corrosion rate as opposed to the Ti billets, which showed much coarser grains, whereas 3-C showed the peak. They also found that grain size, texture orientation, and grain boundary character are all strongly correlated with corrosion rate. Furthermore, they came to the conclusion that using processing routes that create UFG but have an off-basal texture can improve corrosion resistance. In contrast, Rifai et al. [92] observed that when they employed the Fe-20%Cr alloy, Ecorr and Icorr improved by augmenting the passes. Moreover, they found that the Tafel polarization curves along route C were more stable than those along routes A and Bc when there were elevated concentrations of HAGBs and increased grain boundary non-homogeneity. It was found by Gebril et al. [93] that route Bc attained substantial results for the amelioration of A356 alloy corrosion resistance as opposed to other routes. They concluded that this was because the structure created via route Bc was more refined than the structure produced via route A.

Figure 7 shows the results of modeling the corrosion behavior of the ZK30 alloy, comprising the corrosion rate and corrosion resistance. For corrosion rate modeling, the outcomes revealed a substantial and elevated correlation, with an R^2 of 0.92, between the true empirical dataset and the predicted dataset. SVR and GPR algorithms exhibited extraordinary performance for data training and testing, which was assured by the RMSE values and R^2 scores presented in Table 5. Considering the modeling of corrosion resistance using SVR and GPR, the R^2-score was in the range of 0.85 to 0.88 for the training set, and 0.69 to 0.77 for the testing set. From the ML models, it was clear that the number of passes had the most major effect on both the corrosion rate and resistance of the ZK30 alloy. The optimum processing parameters for the ZK30 alloy were 4-Bc using the 90°-die, which reduced the corrosion rate to 0.14 mpy (the corrosion rate of the AA billets was 17.2 mpy). Besides, using 1-P with the 120°-die resulted in an increase in the corrosion resistance of the ZK30 up to 1101 $\Omega \cdot cm^2$ (the corrosion resistance of the AA billets was 69.2 $\Omega \cdot cm^2$.

Table 5. Model evaluation metrics of ZK30 alloy corrosion properties.

Parameter	Algorithm	Training Set		Testing Set	
		RMSE	R^2	RMSE	R^2
Corrosion	SVR	0.0547	0.92	0.0741	0.92
Rate (mpy)	GPR	0.0567	0.92	0.0653	0.93
Corrosion	SVR	103.77	0.85	157.24	0.77
resistance (Ω)	GPR	102.30	0.88	160.01	0.69

3.2.3. Microhardness

The AA billets exhibited a Vicker's microhardness (HV) of 52. Processing through 1-P with the adoption of a 90°-die led to an augmentation in the HV value up to 85. Increases the passes to four with A, Bc, and C led to an increase in hardness of 75%, 81%, and 77%, respectively, compared to the AA counterpart. For the 120°-die, 1-P revealed an augmentation in the HV value of 59% compared to AA billets. Further processing through 4-Bc using the 120°-die exhibited an augmentation in the HV value by 79% compared to AA.
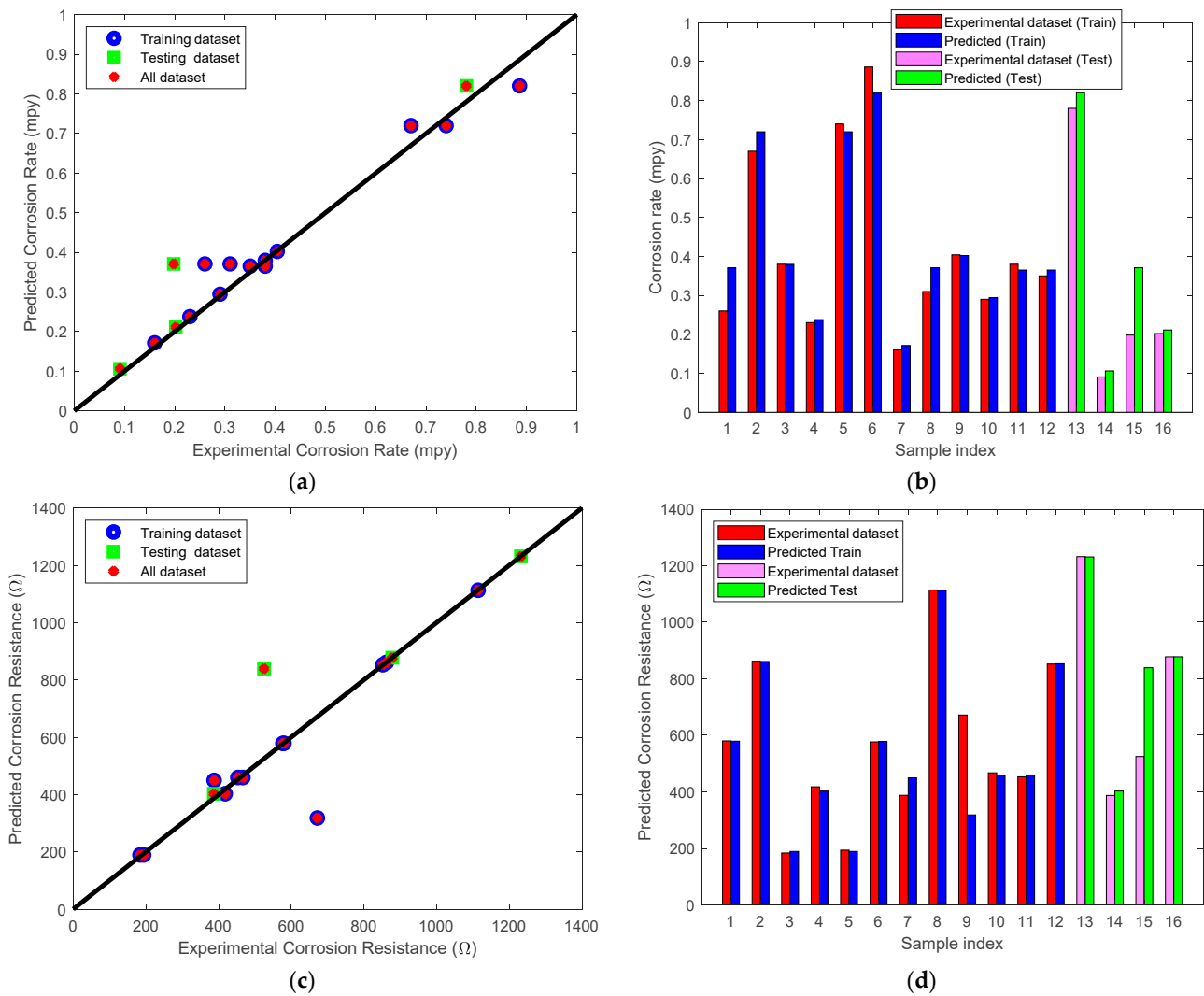
Figure 7. (**a**) Predicted corrosion rate against experimentally measured corrosion rate assessed for the training and the testing datasets, (**b**) Predicted grain size against sample indices for predicted train, predicted test, and experimental dataset. (**c**) Predicted corrosion resistance against empirically measured corrosion resistance assessed for the training and the testing datasets, (**d**) Predicted corrosion resistance against sample indices for predicted train, predicted test, and experimental dataset.

Figure 3 shows that grain refinement is accountable for the higher Vicker's hardness values (HV-values) of the billets obtained from ECAP as opposed to AA. Moreover, as seen in Figure 3d, the HV-values increased as a result of the UFG structure attained with 4-Bc, suggesting that the grain refinement strengthening mechanism was the prevailing one responsible for augmenting the strength of the texture. This was the case because the imposed strain increased with the increase in ECAP passes. It is important to note that additional ECAP passes increased the dislocation density and hence hindered the dislocation motion [59]. According to a previous study [94], strain hardening is an essential factor in strengthening the Mg alloys obtained from ECAP, thus elevating the HV-values. In line with previous research findings [28,29], ECAP processing significantly strengthened the ZK30 alloy via both grain boundary and strain hardening strengthening. Nevertheless, substantial variations in hardness values were not noted across all the tested ECAP routes, similarly to the findings of Sankuru et al. [55], where they showed that 4-Bc was proven to be the ultimate effective method for enhancing the hardness of pure Mg. According to Illgen et al. [95], the best approach is route Dc, which entails rotating the sample by 90° in the same direction between successive passes. The higher HV-values following ECAP

processing are consistent with this finding and also validate the Hall–Petch relationship. The higher dislocation density is responsible for the ECAP-induced post-processing refinement of grains [55]. As was previously documented [28,29], ECAP processing with numerous passes gradually transformed the LAGBs into HAGBs, which is associated with the improvement of UFG. When a UFG structure forms, it increases the size of the grain boundary, which acts as a barrier against dislocation motion. This is consistent with [96,97], which confirmed that increasing the alloy's hardness also enhances its strength.

The microhardness properties of the ZK30 alloy were modeled and evaluated using SVM and GPR. According to Figure 8 and Table 6, both the training and testing sets of microhardness indicated that the expected values were within a hair's breadth of the empirical data. These results were obtained by optimizing SVM and GPR models to meet the conditions for a model with recognized precision that should attain acceptable scores for the training and testing sets alike. For the training dataset, the best-fit models achieved R^2 scores in the range of 0.92 and 0.99; on the other hand, the scores for the testing dataset were in the range of 0.93 and 0.99. This indicates the capabilities of SVM and GRP to effectively grasp the trends in the microhardness data, and implies that they lend themselves well to a generalized predictive model. Similar to the empirical outcomes, the number of passes revealed a higher effect on the HV values, as it displayed a strong correlation of 0.76 (Figure 3). In addition, the die angle exhibited a good negative correlation of 0.37, while the route type revealed an insignificant effect on the HV value as it showed a relatively weak correlation of 0.14. Furthermore, the ML model revealed that the optimum processing conditions for increasing the HV value were 5-Bc through the 120°-die (HV= 98), while the best processing condition for the 90°-die was 4-Bc, which displayed an HV of 93.
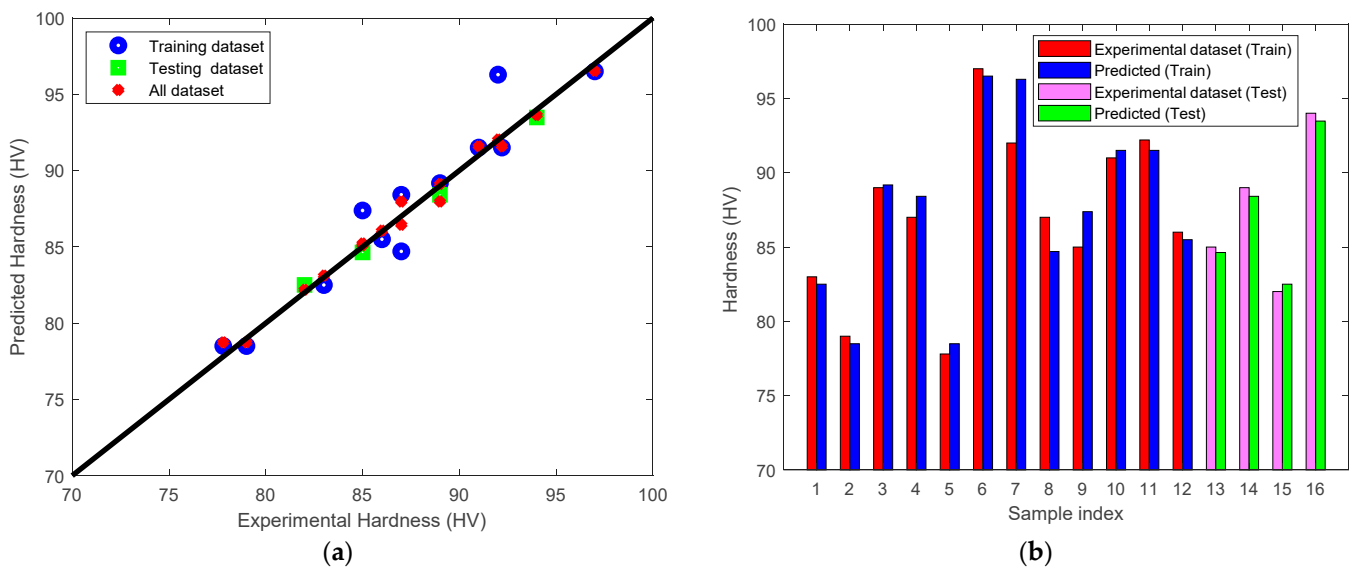

Figure 8. (**a**) Predicted experimental hardness assessed for the training and the testing datasets, (**b**) Predicted hardness against sample indices for predicted train, predicted test, and experimental dataset.

Table 6. Microhardness predictive model evaluation metrics of ZK30 alloy.

ML Algorithm	Training Set		Testing Set	
	RMSE	R^2	RMSE	R^2
Gaussian process regression	0.5593	0.99	1.4007	0.93
Support vector regression	1.4641	0.90	0.0142	0.98

3.2.4. Tensile Properties

Figure 9 reveals the stress-strain diagrams of ZK30 billet samples pre- and post-ECAP processing, which takes place under varied conditions. Figures 10 and 11 demonstrate

the results of the predictive modeling of ZK30 tensile properties, including σy, σu, and El. The tensile findings showed that ECAP-processed ZK30 billets significantly outperformed their AA counterparts in terms of σy and σu without suffering from a significant decrease in El. In addition, it was demonstrated that the highest σy could be obtained at four passes under processing conditions comprising an angle of 90° for the die of ECAP and route Bc, which might be associated with the observed grain refinement (Figure 3). It is possible that the UFG acquired by ECAP processing with many passes is the major cause of the dislocation movement being slowed down [59]. As a result, the process of grain refinement is the strengthening mechanism mainly responsible for the improvement in mechanical properties. Moreover, the use of an angle of 90° for the die of ECAP generated a substantial enhancement in σy, which might be attributable to the resulting augmentation in plastic strain. In addition, the shear strain buildup that occurs as a result of processing to four passes might be related to the augmentation in dislocation density, which impedes the mobility of the dislocation motion [98,99]. As reported by Alateyah et al. [28,29], the increased volume fraction of the HAGBs evaluated via 4-Bc compared to 4-A and 4-C played a significant role in strengthening the ZK30 billets processed using the 90°-die. In addition, the ECAP processing may have contributed to grain refining, which may account for the lowered El. Furthermore, improved El was seen at 1P and 4-Bc when the die angle of 120° was employed in comparison to 1P and 4-Bc when the die angle of 90° was employed. This difference might be related to compelling less strain, as stated by [29]. When compared to routes A and C, which were the other two varieties investigated, route Bc showed the lowest El since it had the most refined grains. Thus, from this vantage point, route Bc may be the most viable option. Similar behavior was reported by Lyszkowski [100] for CuZn36 alloy and by Alateyah et al. [101] for Cu.
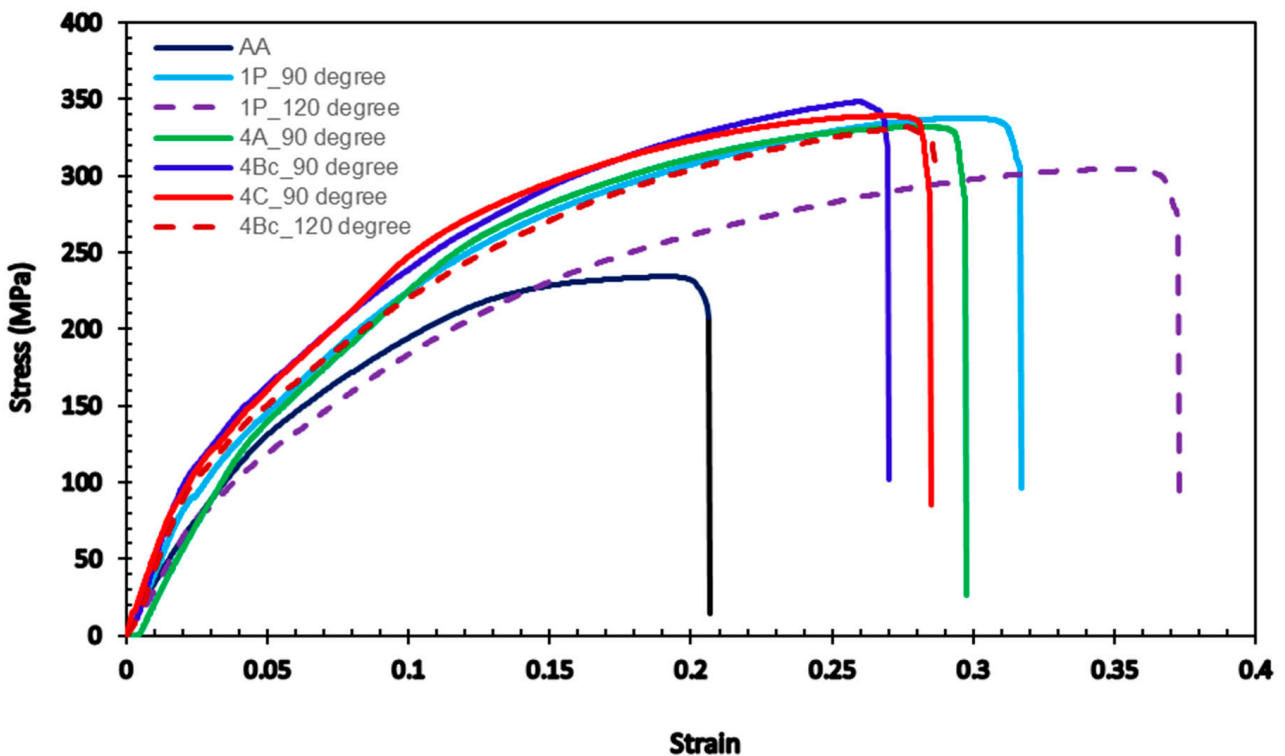

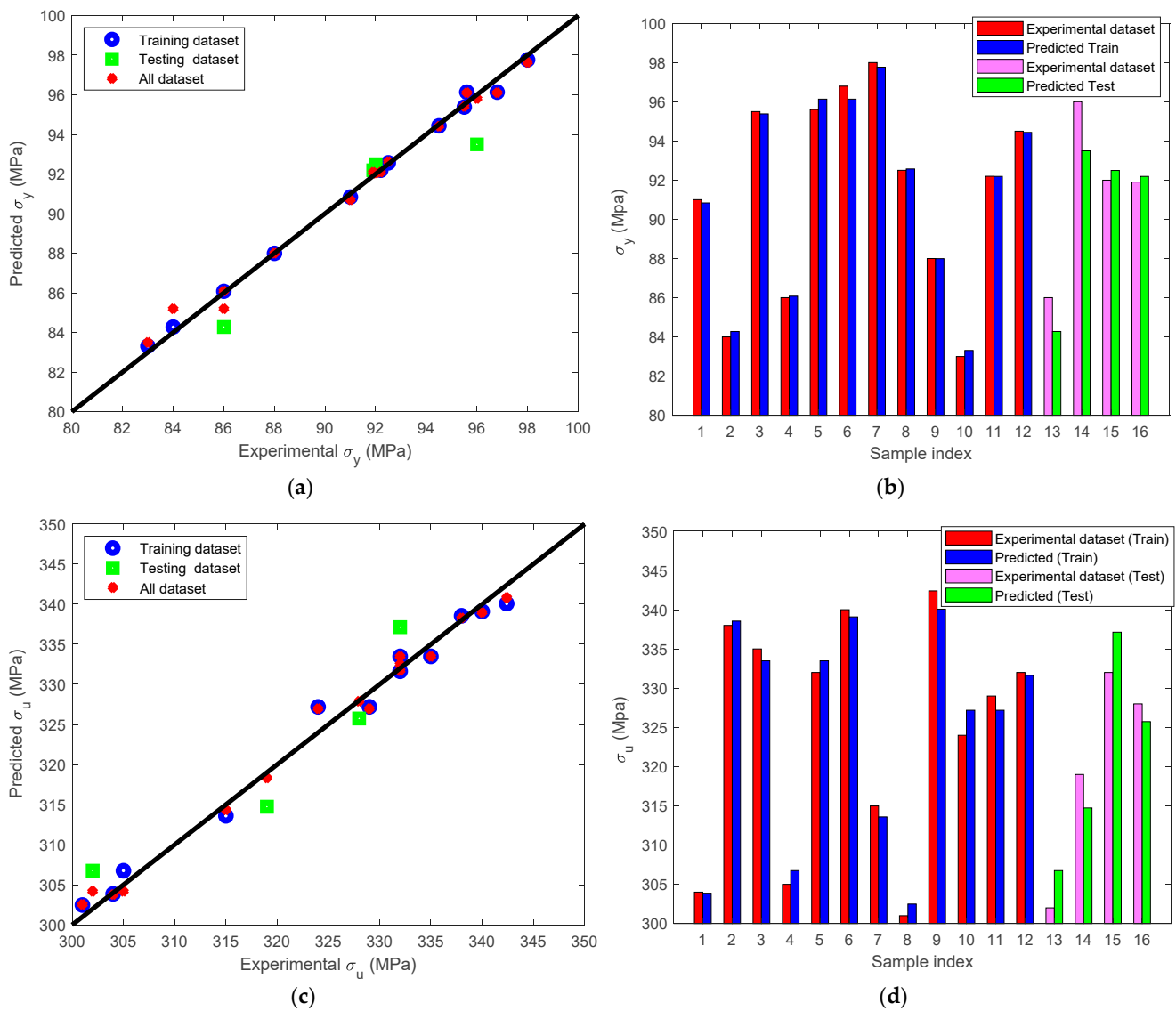**Figure 9.** The stress-strain diagrams of ZK30 billets before and after ECAP processing.

(a)

(b)

(c)

(d)

Figure 10. (**a**) Predicted against experimental σy assessed for the training and the testing datasets, (**b**) Predicted σy against sample indices for predicted train, predicted test, and experimental dataset. (**c**) Predicted against empirical σu assessed for the training and the testing datasets, (**d**) Predicted σu against sample indices for predicted train, predicted test, and experimental dataset.

The Hall–Petch relationship demonstrated that the grain boundary process predominated over the texture strengthening process. Therefore, it is not surprising that augmenting the number of passes resulted in a large reduction in grain size and a corresponding rise in σu. As demonstrated in Figure 3, the creation of finer grains occurs as a result of the LAGBs being absorbed and eventually changing into more stable HAGBs as the applied strain accumulates through an increase in the number of processing passes [35,102]. In addition, Cheng et al. observed that grain refining increases the grain boundaries (GBs) area, which acts as a significant barrier to dislocation motion and boosts the Mg billets' σu [96]. The results are consistent with what was seen in the work of Dumitru et al. [74], who argue that an increase in σu might have been caused by an augmentation in both the dislocation density and the number of second-phase particles due to increasing the number of ECAP passes. The modest rise in σu after the second pass may have resulted from dynamic recrystallization, which in turn eliminated dislocations. Strain softening caused by static recrystallization between ECAP passes can potentially cause a little boost to the σu. Furthermore, the bimodal grain structure revealed in Figure 3 explains the

enhanced El. Previous research [103,104] found that substantial grains (about 20 μm) revealed significant strain deformation by providing strain hardening, whereas small grains (smaller than 5 μm) resulted in an augmentation in strength. This suggests that the ZK30 ECAP-processed billets' El can be enhanced by the combination of special texturing and basal slip [28,29]. Furthermore, the enhancement of grain boundary sliding due to the rise of HAGBs following ECAP processing explains the improvement in the El. The researchers Alateyah et al. [35] found the same thing for pure Mg. Similarly, Jin et al. [105] found that adopting ECAP at elevated temperature reaching up to 250 °C improved the AZ31 alloy by 14%. Similar increases in El were found for AZ31B by Meyer et al. [106] and Agnew et al. [107], who also saw a drop in the σy while the σu remained unchanged. Mostaed et al. [59] showed that the El of ZK60 alloy had increased by 30 percent. In the case of AM80 alloys, Naik et al. [108] found a similar pattern. In light of the previous discoveries about the mechanical behavior of ZK30, it was abundantly obvious that the refinement obtained through ECAP acts as an essential part of the bid to strengthen the magnesium alloy. Sankuru et al. [55] discovered the same result, where an enhancement in the σy, σu, and El of pure Mg following ECAP processing was clearly noted. Additionally, they exposed that the best way to increase σy was via route Bc, whereas the best way to increase σu was via route BA. However, improvement in pure Mg's El was achieved most effectively via route C. Moreover, they mentioned that the tensile properties of the ECAP-processed billets were significantly altered after the first pass, but that successive passes had only a negligible impact on the mechanical properties. They explained that most of the deformation occurs throughout the initial basal slip clutches, while further passes activate non-basal slip systems and hence need less deformation energy. In addition, after ECAP processing, second-phase particles were found consistently and homogeneously distributed at grain boundaries and triple conjunction points, where they notably bolstered the AZ61 alloy's strength, as reported by Shana et al. [76].
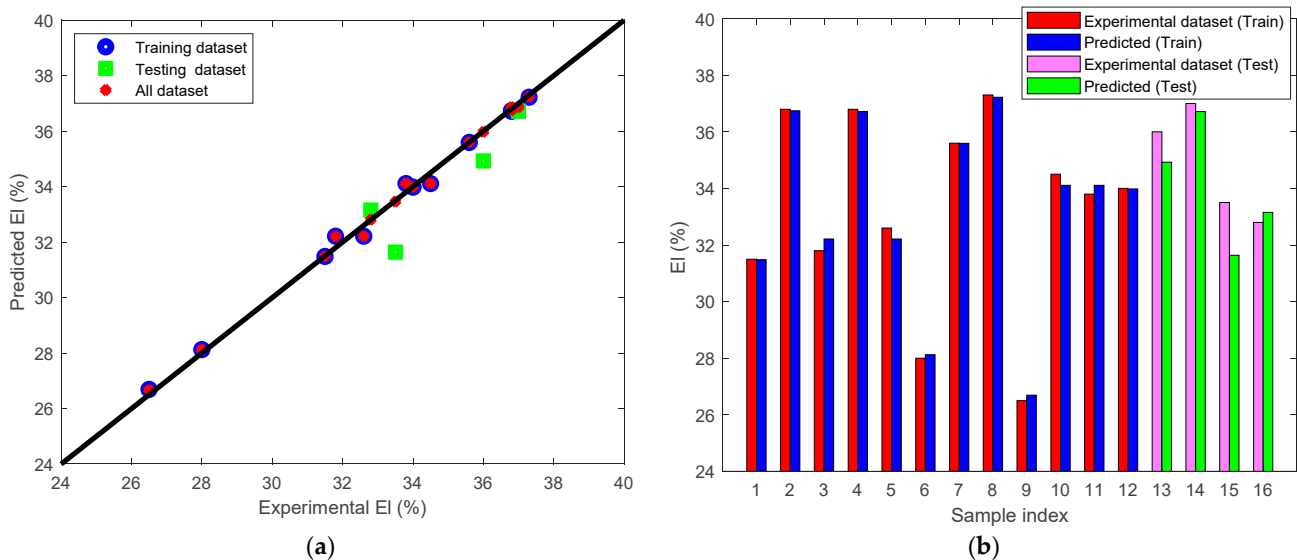

Figure 11. (**a**) Predicted against experimental El assessed for the training and the testing datasets, (**b**) Predicted El against sample indices for predicted train, predicted test, and experimental dataset.

Figure 10 exhibits the outcomes of modeling σy and σu of the ZK30 alloy, Figure 11 exhibits the outcomes of modeling El. The outcomes exposed a substantial association between the practical empirical and prospective outcomes for the datasets. The majority of the adopted algorithms demonstrated satisfactory performance with data training as well as testing, as evidenced by the RMSE and R^2-scores illustrated in Table 7. It is worth mentioning that SVM as well as GPR demonstrated the greatest performance for modeling the process parameters, which were evaluated based on both RMSE and R^2 criteria. This is owing to their intrinsic merits that appear when dealing with nonlinear modeling, making

connections without being bogged down with the local minima of the cost functions. This is consistent with relevant literature since SVM employs the Structural Risk Minimization (SRM) inductive principle, which has been found to outperform conventional methods. The tensile properties of alloys might exhibit nonlinear behavior, which provides widely scattered and statistically spread data. As a result, the mechanical properties of ZK30 alloys are highly dependent on manufacturing factors, which may be modified for specific purposes. In this context, ML modeling techniques excel at tackling both linear and nonlinear multivariate regression issues. From ML models, it was clear the die angle was the most effective processing parameter in improving both σy and σu as it revealed a strong correlation of negative 0.63 and 0.65, respectively. Furthermore, the number of passes revealed a strong correlation of 0.45 and 0.58, respectively, whereas the route type showed an insignificant effect on both σy and σu (Figure 2). For El, the number of passes was the most effective route, recording a strong correlation of negative 0.57, followed by the die angle, which recorded a strong correlation of 0.48. To strengthen the ZK30 alloy, the optimum processing parameters of ECAP were 4-Bc when adopting a 90° channel angle, which led to increasing the σy and σu up to 96 and 342, respectively. On the other hand, to improve the El, 1P using the 120°-die was the optimum processing parameter as it displayed an El of 37.

Table 7. Evaluation metrics of ZK30 tensile properties ML models.

Properties	Algorithm	Training Set		Testing Set	
		RMSE	R^2	RMSE	R^2
σ_y (MPa)	GPR	0.2906	0.99	1.5464	0.81
σ_u (MPa)	GPR	1.6323	0.98	4.2525	0.86
El (%)	SVM	1.6524	0.93	1.4570	0.82

3.3. ML Model Deployment

ML model deployment refers to the process of placing a finalized, trained, and verified ML model into a production setting where it can be used and updated easily. Systems that use ML in production are complex software systems that require regular upkeep. This presents developers with new challenges, some of which are shared with the operation of conventional software services, while others are unique to ML. As a result, most ML research field models were not put to use. The need for data storage, high computational costs, a lack of control and ownership, difficulties in reproducibility, and a severe shortage of well-defined standards are all factors contributing to this challenging environment [109–111]. Users can benefit from models in a variety of contexts, and developers often expose them to apps via an Application Programming Interface (API). Gradio [112] is an open-source Python module that makes it easier to create APIs by providing methods and functions for adding input spaces and facilities to a graphical user interface (GUI) for the deployed model. The fact that Gradio can be installed on the host server is yet another plus for using it. Hugging Face [113] is an open-source hosting platform for machine learning models, transforming them from models in papers into functional objects that can be effectively utilized. For this purpose, as shown in Figure 12, a GUI tool was developed in Python using the Gradio library, to expect the mechanical properties of ZK30 alloys when adopting ECAP parameters. This tool is hosted on the Hugging Face platform. This web app presents the three input parameters (N, φ, and Rt) in line with the suggested ML model. Users may enter values for the ECAP parameters and submit them to get the expected values of the ZK30 properties, comprising microhardness, tensile properties, grain size, and corrosion properties based on SVR and GPR algorithms.
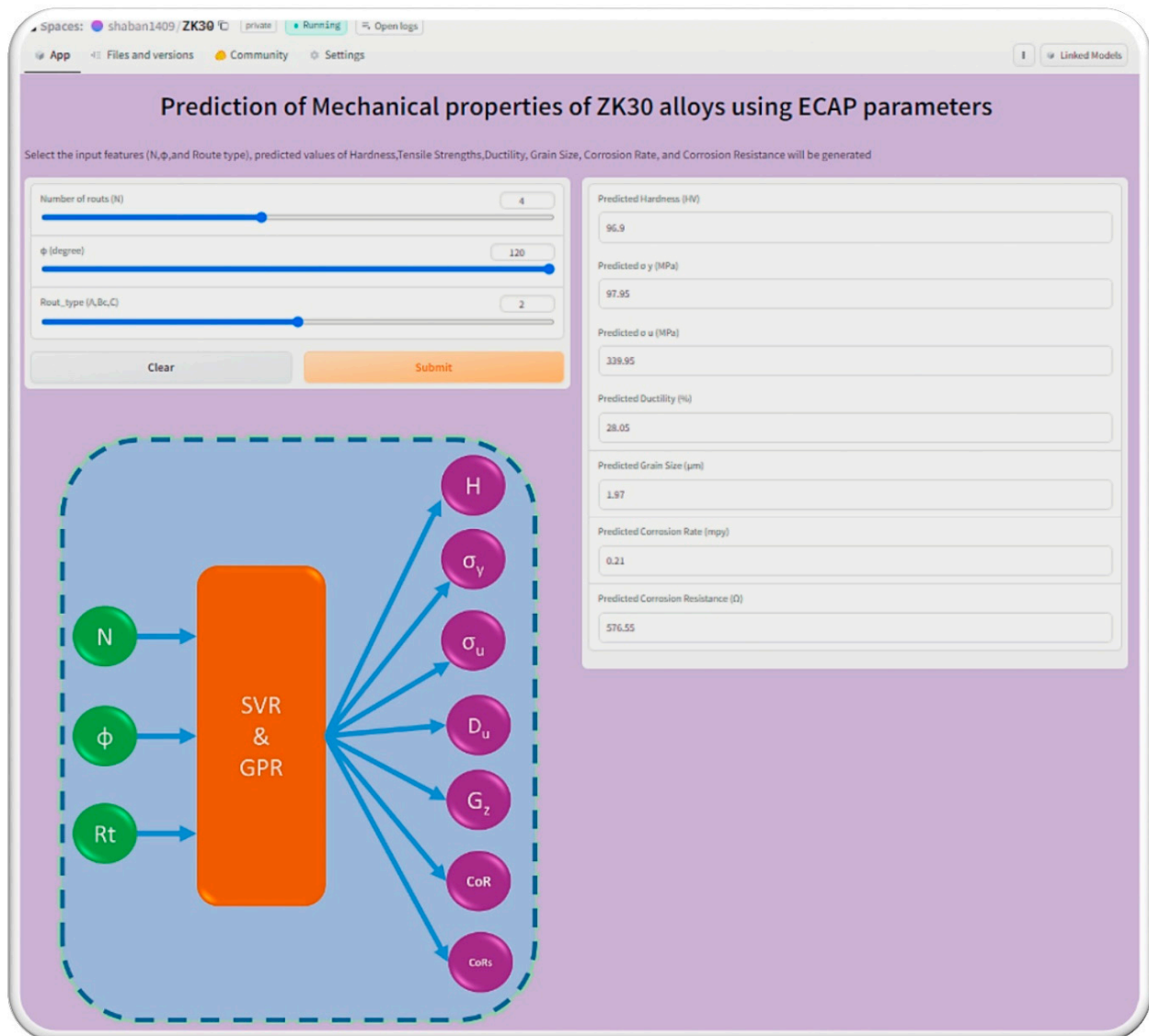
Figure 12. Illustration image of web application used for model deployment.

4. Conclusions

In this work, experimental investigations were conducted on billets of ZK30 alloy to determine the ECAP processing conditions that correspond to optimum alloy performance. The attributes under investigation were the alloy's microstructural evolution, its crystallographic texture development, and its electrochemical and mechanical properties. ML was employed to build prediction models that optimize the ECAP's processing parameters towards best alloy performance. The following can be concluded:

1. The adopted ML models can be trusted, as the outcomes they generated were consistent with those of the experimental results.
2. The ML model confirms the optimum ECAP processing parameters for grain refinement found experimentally, namely using the 4-Bc path with a die angle of 120°.
3. The maximum texture intensity realized was 20.8 times random, produced by 1P processing using the 90°-die.
4. Finer grain sizes lead to lower corrosion rates. The ML model confirms this, and also confirms the experiment's findings that the lowest corrosion rate was achieved in the 90°-die via the 4-Bc processing condition.
5. The highest corrosion resistance of 1101 $\Omega \cdot cm^2$ is achieved using 1-Pass ECAP processing at 120°-die.

6. The ML model predicts that the highest hardness values should occur with 5-Bc processing with a die angle of 120°. This is in agreement with the experimental results (HV = 98).
7. The greatest strengthening effect is produced by ECAP processing via 4-Bc and using a die angle of 90°. The highest σy and σu achieved were 96 and 342 MPa, respectively.

Author Contributions: Conceptualization, W.H.E.-G., A.I.A., H.G.S. and M.S.; methodology, A.I.A., W.H.E.-G., M.F.A., M.O.A. and A.B.; software, F.N.A. and M.K.; validation, W.H.E.-G., M.S. and H.G.S.; formal analysis, A.I.A., F.N.A. and M.F.A.; investigation, M.O.A. and A.B.; resources, A.I.A., W.H.E.-G. and M.O.A.; data curation, H.G.S. and M.S.; writing—original draft preparation, M.K., A.I.A. and M.S.; writing—review and editing, W.H.E.-G. and H.G.S., visualization, M.O.A. and A.B., M.F.A. and F.N.A. supervision, A.I.A., H.G.S. and M.F.A.; project administration, W.H.E.-G., A.I.A. and M.O.A. All authors have read and agreed to the published version of the manuscript.

Institutional Review Board Statement: Not applicable.

Informed Consent Statement: Not applicable.

Data Availability Statement: All the raw data supporting the conclusion of this paper were provided by the authors.

Conflicts of Interest: The authors declare no conflict of interest.

References

1. Kulekci, M.K. Magnesium and its alloys applications in automotive industry. *Int. J. Adv. Manuf. Technol.* **2008**, *39*, 851–865. [CrossRef]
2. Friedrich, H.; Schumann, S. Research for a 'new age of magnesium' in the automotive industry. *J. Mater. Process. Technol.* **2001**, *117*, 276–281. [CrossRef]
3. Li, N.; Zheng, Y. Novel Magnesium Alloys Developed for Biomedical Application: A Review. *J. Mater. Sci. Technol.* **2013**, *29*, 489–502. [CrossRef]
4. Chen, Y.; Xu, Z.; Smith, C.; Sankar, J. Recent advances on the development of magnesium alloys for biodegradable implants. *Acta Biomater.* **2014**, *10*, 4561–4573. [CrossRef]
5. Gu, X.-N.; Zheng, Y.-F. A review on magnesium alloys as biodegradable materials. *Front. Mater. Sci. China* **2010**, *4*, 111–115. [CrossRef]
6. Saris, N.-E.L.; Mervaala, E.; Karppanen, H.; Khawaja, J.A.; Lewenstam, A. Magnesium: An update on physiological, clinical and analytical aspects. *Clin. Chim. Acta* **2000**, *294*, 1–26. [CrossRef]
7. Okuma, T. Magnesium and bone strength. *Nutrition* **2001**, *17*, 679–680. [CrossRef]
8. Wolf, F.I.; Cittadini, A. Chemistry and biochemistry of magnesium. *Mol. Asp. Med.* **2003**, *24*, 3–9. [CrossRef]
9. Staiger, M.P.; Pietak, A.M.; Huadmai, J.; Dias, G. Magnesium and its alloys as orthopedic biomaterials: A review. *Biomaterials* **2006**, *27*, 1728–1734. [CrossRef]
10. Yin, Y.; Huang, Q.; Liang, L.; Hu, X.; Liu, T.; Weng, Y.; Long, T.; Liu, Y.; Li, Q.; Zhou, S.; et al. In vitro degradation behavior and cytocompatibility of ZK30/bioactive glass composites fabricated by selective laser melting for biomedical applications. *J. Alloys Compd.* **2019**, *785*, 38–45. [CrossRef]
11. Lin, X.; Tan, L.; Zhang, Q.; Yang, K.; Hu, Z.; Qiu, J.; Cai, Y. The in vitro degradation process and biocompatibility of a ZK60 magnesium alloy with a forsterite-containing micro-arc oxidation coating. *Acta Biomater.* **2013**, *9*, 8631–8642. [CrossRef] [PubMed]
12. Yamasaki, Y.; Yoshida, Y.; Okazaki, M.; Shimazu, A.; Kubo, T.; Akagawa, Y.; Uchida, T. Action of FGMgCO3Ap-collagen composite in promoting bone formation. *Biomaterials* **2003**, *24*, 4913–4920. [CrossRef]
13. Zreiqat, H.; Howlett, C.R.; Zannettino, A.; Evans, P.; Schulze-Tanzil, G.; Knabe, C.; Shakibaei, M. Mechanisms of magnesium-stimulated adhesion of osteoblastic cells to commonly used orthopaedic implants. *J. Biomed. Mater. Res.* **2002**, *62*, 175–184. [CrossRef]
14. Kirkland, N.T. Magnesium biomaterials: Past, present and future. *Corros. Eng. Sci. Technol.* **2012**, *47*, 322–328. [CrossRef]
15. Kannan, M.B.; Raman, R.K.S. In vitro degradation and mechanical integrity of calcium-containing magnesium alloys in modified-simulated body fluid. *Biomaterials* **2008**, *29*, 2306–2314. [CrossRef]
16. Li, Z.; Song, G.-L.; Song, S. Effect of bicarbonate on biodegradation behavior of pure magnesium in a simulated body fluid. *Electrochim. Acta* **2014**, *115*, 56–65. [CrossRef]
17. Song, G. Control of biodegradation of biocompatable magnesium alloys. *Corros. Sci.* **2007**, *49*, 1696–1701. [CrossRef]

18. Song, Y.W.; Shan, D.Y.; Han, E.H. Electrodeposition of hydroxyapatite coating on AZ91D magnesium alloy for biomaterial application. *Mater. Lett.* **2008**, *62*, 3276–3279. [CrossRef]

19. El-Garaihy, W.H.; Alateyah, A.I.; Alawad, M.O.; Aljohani, T.A. Improving the Corrosion Behavior and Mechanical Properties of Biodegradable Mg-Zn-Zr Alloys Through ECAP for Usage in Biomedical Applications. In *Magnesium Technology*; Springer: Cham, Switzerland, 2022; pp. 259–269. Available online: https://link.springer.com/chapter/10.1007/978-3-030-92533-8_45 (accessed on 5 February 2022).

20. Hornberger, H.; Virtanen, S.; Boccaccini, A.R. Biomedical coatings on magnesium alloys—A review. *Acta Biomater.* **2012**, *8*, 2442–2455. [CrossRef]

21. Sun, Y.; Zhang, B.; Wang, Y.; Geng, L.; Jiao, X. Preparation and characterization of a new biomedical Mg–Zn–Ca alloy. *Mater. Des.* **2012**, *34*, 58–64. [CrossRef]

22. Alateyah, A.I.; Aljohani, T.A.; Alawad, M.O.; Elkatatny, S.; El-Garaihy, W.H. Improving the Corrosion Behavior of Biodegradable AM60 Alloy through Plasma Electrolytic Oxidation. *Metals* **2021**, *11*, 953. [CrossRef]

23. Almenaif, O.; Alhumaydan, Y.; Alnafisah, M.; Aldhalaan, M.; Alateyah, A.I.; El-Garaihy, W.H. A Computational Investigation into the Effect of Equal Channel Angular Processing on the Mechanical Properties of Severely Deformed ZK 60 Alloy Validated by Experiments. *Am. J. Eng. Appl. Sci.* **2020**, *13*, 296–310. [CrossRef]

24. Zong, Y.; Yuan, G.; Zhang, X.; Mao, L.; Niu, J.; Ding, W. Comparison of biodegradable behaviors of AZ31 and Mg–Nd–Zn–Zr alloys in Hank's physiological solution. *Mater. Sci. Eng. B* **2012**, *177*, 395–401. [CrossRef]

25. Ng, W.F.; Wong, M.H.; Cheng, F.T. Stearic acid coating on magnesium for enhancing corrosion resistance in Hanks' solution. *Surf. Coat. Technol.* **2010**, *204*, 1823–1830. [CrossRef]

26. Hermawan, H.; Dubé, D.; Mantovani, D. Developments in metallic biodegradable stents. *Acta Biomater.* **2010**, *6*, 1693–1697. [CrossRef]

27. Gunde, P.; Hänzi, A.C.; Sologubenko, A.S.; Uggowitzer, P.J. High-strength magnesium alloys for degradable implant applications. *Mater. Sci. Eng. A* **2011**, *528*, 1047–1054. [CrossRef]

28. Alateyah, A.I.; Alawad, M.O.; Aljohani, T.A.; El-Garaihy, W.H. Effect of ECAP Route Type on the Microstructural Evolution, Crystallographic Texture, Electrochemical Behavior and Mechanical Properties of ZK30 Biodegradable Magnesium Alloy. *Materials* **2022**, *15*, 6088. [CrossRef]

29. Alateyah, A.I.; Alawad, M.O.; Aljohani, T.A.; El-Garaihy, W.H. Influence of Ultrafine-Grained Microstructure and Texture Evolution of ECAPed ZK30 Magnesium Alloy on the Corrosion Behavior in Different Corrosive Agents. *Materials* **2022**, *15*, 5515. [CrossRef]

30. Rodrigues, J.D.S.; Antonini, L.M.; Bastos, A.A.C.; Zhou, J.; Malfatti, C.F. Corrosion resistance and tribological behavior of ZK30 magnesium alloy coated by plasma electrolytic oxidation. *Surf. Coat. Technol.* **2021**, *410*, 126983. [CrossRef]

31. Wang, Y.; Guan, S.; Zeng, X.; Ding, W. Effects of RE on the microstructure and mechanical properties of Mg–8Zn–4Al magnesium alloy. *Mater. Sci. Eng. A* **2006**, *416*, 109–118. [CrossRef]

32. Witte, F.; Hort, N.; Vogt, C.; Cohen, S.; Kainer, K.U.; Willumeit, R.; Feyerabend, F. Degradable biomaterials based on magnesium corrosion. *Curr. Opin. Solid State Mater. Sci.* **2008**, *12*, 63–72. [CrossRef]

33. Gu, X.; Zheng, Y.; Cheng, Y.; Zhong, S.; Xi, T. In vitro corrosion and biocompatibility of binary magnesium alloys. *Biomaterials* **2009**, *30*, 484–498. [CrossRef]

34. Alateyah, A.I.; Aljohani, T.; Alawad, M.; El-Hafez, H.; Almutairi, A.; Alharbi, E.; Alhamada, R.; El-Garaihy, B.; El-Garaihy, W. Improved Corrosion Behavior of AZ31 Alloy through ECAP Processing. *Metals* **2021**, *11*, 363. [CrossRef]

35. Alateyah, A.I.; Ahmed, M.M.; Alawad, M.O.; Elkatatny, S.; Zedan, Y.; Nassef, A.; El-Garaihy, W. Effect of ECAP die angle on the strain homogeneity, microstructural evolution, crystallographic texture and mechanical properties of pure magnesium: Numerical simulation and experimental approach. *J. Mater. Res. Technol.* **2022**, *17*, 1491–1511. [CrossRef]

36. Elkhodary, K.I.; Salem, G.S.; Zikry, M.A. Equal Channel Angular Pressing of Canned 2124-Al Compacts: Processing, Experiments, and Modeling. *Met. Mater. Trans. A* **2008**, *39*, 2184–2192. [CrossRef]

37. El-Garaihy, W.H.; Fouad, D.M.; Salem, H.G. Multi-channel Spiral Twist Extrusion (MCSTE): A Novel Severe Plastic Deformation Technique for Grain Refinement. *Met. Mater. Trans. A* **2018**, *49*, 2854–2864. [CrossRef]

38. Fouad, D.M.; Moataz, A.; El-Garaihy, W.H.; Salem, H.G. Numerical and experimental analysis of multi-channel spiral twist extrusion processing of AA5083. *Mater. Sci. Eng. A* **2019**, *764*, 138216. [CrossRef]

39. Fouad, D.M.; El-Garaihy, W.H.; Ahmed, M.M.Z.; Seleman, M.M.E.; Salem, H.G. Influence of multi-channel spiral twist extrusion (MCSTE) processing on structural evolution, crystallographic texture and mechanical properties of AA1100. *Mater. Sci. Eng. A* **2018**, *737*, 166–175. [CrossRef]

40. Fouad, D.M.; El-Garaihy, W.H.; Ahmed, M.M.Z.; Albaijan, I.; Seleman, M.M.E.; Salem, H.G. Grain Structure Evolution and Mechanical Properties of Multi-Channel Spiral Twist Extruded AA5083. *Metals* **2021**, *11*, 1276. [CrossRef]

41. Alvarez-Lopez, M.; Pereda, M.D.; Del Valle, J.A.; Fernandez-Lorenzo, M.; Garcia-Alonso, M.C.; Ruano, O.A.; Escudero, M.L. Corrosion behavior of AZ31 magnesium alloy with different grain sizes in simulated biological fluids. *Acta Biomater.* **2010**, *6*, 1763–1771. [CrossRef]

42. El-Shenawy, M.; Ahmed, M.M.Z.; Nassef, A.; El-Hadek, M.; Alzahrani, B.; Zedan, Y.; El-Garaihy, W.H. Effect of ECAP on the Plastic Strain Homogeneity, Microstructural Evolution, Crystallographic Texture and Mechanical Properties of AA2xxx Aluminum Alloy. *Metals* **2021**, *11*, 938. [CrossRef]

43. Gao, J.H.; Guan, S.K.; Ren, Z.W.; Sun, Y.F.; Zhu, S.J.; Wang, B. Homogeneous corrosion of high-pressure torsion treated Mg–Zn–Ca alloy in simulated body fluid. *Mater. Lett.* **2011**, *65*, 691–693. [CrossRef]

44. El-Garaihy, W.H.; Rassoul, E.A.; Alateyah, A.; Alaskari, A.M.; Oraby, S. Data Manipulation Approach and Parameters Inter-relationships of the High-Pressure Torsion for AA6061-15%SiCp Composite. *SAE Int. J. Mater. Manuf.* **2018**, *11*, 167–182. [CrossRef]

45. El-Garaihy, W.; Rassoul, E.S.M.; Salem, H.G. Consolidation of High Performance AA6061 and AA6061-SiCp Composite Processed by High Pressure Torsion. *Mater. Sci. Forum* **2014**, *783–786*, 2623–2628. [CrossRef]

46. Alateyah, A.I.; Alharbi, M.; El-Hafez, H.M.; El-Garaihy, W.H. The Effect of Equal-Channel Angular Pressing Processing on Microstructural Evolution, Hardness Homogeneity, and Mechanical Properties of Pure Aluminum. *SAE Int. J. Mater. Manuf.* **2020**, *14*, 113–125. [CrossRef]

47. Salem, H.G. *Influence of Equal Channel Angular Extrusion Processing on the Physical, Mechanical, and Microstructural Properties of Al-Cu-Li Base Alloys*; Texas A&M University, ProQuest Dissertations Publishing: College Station, TX, USA, 1997.

48. Wu, W.J.; Chen, W.; Zhang, L.; Chen, X.; Wang, H.; Wang, W.; Zhang, W. Improvement of tension/compression asymmetry for high-performance ZK61 magnesium alloy rod via tailoring deformation parameters: Upsetting-extrusion temperature and upsetting ratio. *Mater. Sci. Eng. A* **2021**, *823*, 141767. [CrossRef]

49. Savaedi, Z.; Mirzadeh, H.; Aghdam, R.M.; Mahmudi, R. Effect of grain size on the mechanical properties and bio-corrosion resistance of pure magnesium. *J. Mater. Res. Technol.* **2022**, *19*, 3100–3109. [CrossRef]

50. Němec, M.; Jäger, A.; Tesař, K.; Gärtnerová, V. Influence of alloying element Zn on the microstructural, mechanical and corrosion properties of binary Mg-Zn alloys after severe plastic deformation. *Mater. Charact.* **2017**, *134*, 69–75. [CrossRef]

51. Minarik, P.; Jablonska, E.; Kral, R.; Lipov, J.; Ruml, T.; Blawert, C.; Hadzima, B.; Chmelík, F. Effect of equal channel angular pressing on in vitro degradation of LAE442 magnesium alloy. *Mater. Sci. Eng. C* **2017**, *73*, 736–742. [CrossRef]

52. Li, X.; Jiang, J.; Zhao, Y.; Ma, A.; Wen, D.; Zhu, Y. Effect of equal-channel angular pressing and aging on corrosion behavior of ZK60 Mg alloy. *Trans. Nonferrous Met. Soc. China* **2015**, *25*, 3909–3920. [CrossRef]

53. Goodman, S.B.; Davidson, J.A.; Fornasier, V.L.; Mishra, A.K. Histological response to cylinders of a low modulus titanium alloy (Ti-13Nb-13Zr) and a wear resistant zirconium alloy (Zr-2.5Nb) implanted in the rabbit tibia. *J. Appl. Biomater.* **1993**, *4*, 331–339. [CrossRef]

54. Valiev, R.Z.; Langdon, T.G. Principles of equal channel angular pressing as a processing tool for grain refinement. *Prog. Mater. Sci.* **2006**, *51*, 881–981. [CrossRef]

55. Sankuru, A.B.; Sunkara, H.; Sethuraman, S.; Gudimetla, K.; Ravisankar, B.; Babu, S.P.K. Effect of processing route on microstructure, mechanical and dry sliding wear behavior of commercially pure magnesium processed by ECAP with back pressure. *Trans. Indian Inst. Met.* **2021**, *74*, 2659–2669. [CrossRef]

56. Orlov, O.; Ralston, K.D.; Birbilis, N.; Estrin, Y. Enhanced corrosion resistance of Mg alloy ZK60 after processing by integrated extrusion and equal channel angular pressing. *Acta Mater.* **2011**, *59*, 6176–6186. [CrossRef]

57. Alawad, M.O.; Alateyah, A.I.; El-Garaihy, W.H.; BaQais, A.; Elkatatny, S.; Kouta, H.; Kamel, M.; El-Sanabary, S. Optimizing the ECAP Parameters of Biodegradable Mg-Zn-Zr Alloy Based on Experimental, Mathematical Empirical, and Response Surface Methodology. *Materials* **2022**, *15*, 7719. [CrossRef]

58. Peron, M.; Skaret, P.C.; Fabrizi, A.; Varone, A.; Montanari, R.; Roven, H.J.; Ferro, P.; Berto, F.; Torgersen, J. The effect of Equal Channel Angular Pressing on the stress corrosion cracking susceptibility of AZ31 alloy in simulated body fluid. *J. Mech. Behav. Biomed. Mater.* **2020**, *106*, 103724. [CrossRef]

59. Mostaed, E.; Hashempour, M.; Fabrizi, A.; Dellasega, D.; Bestetti, M.; Bonollo, F.; Vedani, M. Microstructure, texture evolution, mechanical properties and corrosion behavior of ECAP processed ZK60 magnesium alloy for biodegradable applications. *J. Mech. Behav. Biomed. Mater.* **2014**, *37*, 307–322. [CrossRef]

60. Gao, M.; Yang, K.; Tan, L.; Ma, Z. Role of bimodal-grained structure with random texture on mechanical and corrosion properties of a Mg-Zn-Nd alloy. *J. Magnes. Alloys* **2021**, *10*, 2147–2157. [CrossRef]

61. Schmidt, J.; Marques, M.R.; Botti, S.; Marques, M.A. Recent advances and applications of machine learning in solid-state materials science. *NPJ Comput. Mater.* **2019**, *5*, 83. [CrossRef]

62. Wen, C.; Zhang, Y.; Wang, C.; Xue, D.; Bai, Y.; Antonov, S.; Dai, L.; Lookman, T.; Su, Y. Machine learning assisted design of high entropy alloys with desired property. *Acta Mater.* **2019**, *170*, 109–117. [CrossRef]

63. Butler, K.T.; Davies, D.W.; Cartwright, H.; Isayev, O.; Walsh, A. Machine learning for molecular and materials science. *Nature* **2018**, *559*, 547–555. [CrossRef]

64. Schleder, G.R.; Padilha, A.C.; Acosta, C.M.; Costa, M.; Fazzio, A. From DFT to machine learning: Recent approaches to materials science—A review. *J. Phys. Mater.* **2019**, *2*, 032001. [CrossRef]

65. Wang, A.Y.; Murdock, R.J.; Kauwe, S.K.; Oliynyk, A.O.; Gurlo, A.; Brgoch, J.; Persson, K.A.; Sparks, T.D. Machine learning for materials scientists: An introductory guide toward best practices. *Chem. Mater.* **2020**, *32*, 4954–4965. [CrossRef]

66. Sarker, I.H. Machine learning: Algorithms, real-world applications and research directions. *SN Comput. Sci.* **2021**, *2*, 160. [CrossRef]

67. Williams, C.K.; Rasmussen, C.E. *Gaussian Processes for Machine Learning*; MIT Press: Cambridge, MA, USA, 2006.

68. Deringer, V.L.; Bartók, A.P.; Bernstein, N.; Wilkins, D.M.; Ceriotti, M.; Csányi, G. Gaussian process regression for materials and molecules. *Chem. Rev.* **2021**, *121*, 10073–10141. [CrossRef]

69. Vapnik, V. *The Nature of Statistical Learning Theory*; Springer Science & Business Media: New York, NY, USA, 1999.
70. Cherkassky, V.; Ma, Y. Practical selection of SVM parameters and noise estimation for SVM regression. *Neural Netw.* **2014**, *17*, 113–126. [CrossRef]
71. Ahmad, A.S.; Hassan, M.Y.; Abdullah, M.P.; Rahman, H.A.; Hussin, F.; Abdullah, H.; Saidur, R. A review on applications of ANN and SVM for building electrical energy consumption forecasting. *Renew. Sustain. Energy Rev.* **2014**, *33*, 102–109. [CrossRef]
72. Blanco, V.; Japón, A.; Puerto, J. A mathematical programming approach to SVM-based classification with label noise. *Comput. Ind. Eng.* **2022**, *172*, 108611. [CrossRef]
73. Ahmed, N.I.; Nasrin, F. Reducing Error Rate for Eye-Tracking System by Applying SVM. In *Machine Intelligence and Data Science Applications*; Springer: New York, NY, USA, 2022; pp. 35–47.
74. Dumitru, F.D.; Higuera-Cobos, O.F.; Cabrera, J.M. ZK60 alloy processed by ECAP: Microstructural, physical and mechanical characterization. *Mater. Sci. Eng. A* **2014**, *594*, 32–37. [CrossRef]
75. Tong, L.B.; Zheng, M.Y.; Hu, X.S.; Wu, K.; Xu, S.W.; Kamado, S.; Kojima, Y. Influence of ECAP routes on microstructure and mechanical properties of Mg–Zn–Ca alloy. *Mater. Sci. Eng. A* **2010**, *527*, 4250–4256. [CrossRef]
76. Shana, Z.; Yang, J.; Fana, J.; Zhang, H.; Zhang, Q.; Wu, Y.; Li, W.; Dong, H.; Xu, B. Extraordinary mechanical properties of AZ61 alloy processed by ECAP with 160° channel angle and EPT. *J. Magnes. Alloy.* **2021**, *9*, 548–559. [CrossRef]
77. Sun, J.; Xu, B.; Yang, Z.; Zhuo, X.; Han, J.; Wu, Y.; Song, D.; Liu, H.; Jiang, J.; Ma, A. Developing an industrial-scale ECAP Mg-Al-Zn alloy with multiheterostructure for synchronously high strength and good ductility. *Mater. Charact.* **2020**, *164*, 110341. [CrossRef]
78. Figueiredo, R.B.; Langdon, T.G. Principles of grain refinement in magnesium alloys processed by equal-channel angular pressing. *J. Mater. Sci.* **2009**, *44*, 4758. [CrossRef]
79. Xu, B.; Sun, J.; Yang, Z.; Xiao, L.; Zhou, H.; Han, J.; Liu, H.; Wu, Y.; Yuan, Y.; Zhuo, H.; et al. Microstructure and anisotropic mechanical behavior of the high-strength and ductility AZ91 Mg alloy processed by hot extrusion and multi-pass RD-ECAP. *Mater. Sci. Eng. A* **2020**, *780*, 139191. [CrossRef]
80. Suh, J.; Hernández, J.V.; Letzig, D.; Golle, R.; Volk, V. Effect of processing route on texture and cold formability of AZ31 Mg alloy sheets processed by ECAP. *Mater. Sci. Eng. A* **2016**, *669*, 159–170. [CrossRef]
81. Fan, G.D.; Zheng, M.Y.; Hu, X.S.; Xu, C.; Wu, K.; Golovin, I.S. Improved mechanical property and internal friction of pure Mg processed by ECAP. *Mater. Sci. Eng. A* **2012**, *556*, 588–594. [CrossRef]
82. Kim, W.J.; An, C.W.; Kim, Y.S.; Hong, S.I. Mechanical properties and microstructures of an AZ61 Mg Alloy produced by equal channel angular pressing. *Scr. Mater.* **2002**, *47*, 39–44. [CrossRef]
83. Gzyl, M.; Rosochowski, A.; Boczkal, S.; Olejnik, L. The role of microstructure and texture in controlling mechanical properties of AZ31B magnesium alloy processed by I-ECAP. *Mater. Sci. Eng. A* **2015**, *638*, 20–29. [CrossRef]
84. Biswas, S.; Singh, D.S.; Beausir, B.; Toth, L.S.; Suwas, S. Thermal Response on the Microstructure and Texture of ECAP and Cold-Rolled Pure Magnesium. *Metall. Mater. Trans. A* **2015**, *46*, 2598–2613. [CrossRef]
85. Akbaripanah, F.; Saniee, F.F.; Mahmudi, R.; Kim, H.K. The influences of extrusion and equal channel angular pressing (ECAP) processes on the fatigue behavior of AM60 magnesium alloy. *Mater. Sci. Eng. A* **2013**, *565*, 308–316. [CrossRef]
86. Xu, S.W.; Zheng, M.Y.; Kamado, S.; Wu, K. The microstructural evolution and superplastic behavior at low temperatures of Mg–5.00Zn–0.92Y–0.16Zr (wt.%) alloys after hot extrusion and ECAP process. *Mater. Sci. Eng. A* **2012**, *549*, 60–68. [CrossRef]
87. Aljohani, T.A.; Alawad, M.O.; Elkatatny, S.; Alateyah, A.I.; Bin Rubayan, M.T.; Alhajji, M.A.; AlBeladi, M.I.; Khoshnaw, F.; El-Garaihy, W.H. Electrochemical Behavior of SiC-Coated AA2014 Alloy through Plasma Electrolytic Oxidation. *Materials* **2022**, *15*, 3724. [CrossRef]
88. Mostaed, E.; Vedani, M.; Hashempour, M.; Bestetti, M. Influence of ECAP process on mechanical and corrosion properties of pure Mg and ZK60 magnesium alloy for biodegradable stent applications. *Biomatter* **2014**, *4*, e28283. [CrossRef] [PubMed]
89. Tang, L.; Zhao, Y.; Islamgaliev, R.K.; Tsao, C.Y.A.; Valiev, R.Z.; Lavernia, E.J.; Zhu, Y.T. Enhanced strength and ductility of AZ80 Mg alloys by spray forming and ECAP. *Mater. Sci. Eng. A* **2016**, *670*, 280–291. [CrossRef]
90. Cubides, Y.; Zhao, D.; Nash, L.; Yadav, D.; Xie, K.; Karaman, I.; Castaneda, H. Effects of dynamic recrystallization and strain-induced dynamic precipitation on the corrosion behavior of partially recrystallized Mg–9Al–1Zn alloys. *J. Magnes. Alloy.* **2020**, *8*, 1016–1037. [CrossRef]
91. Gurao, N.B.; Manivasagam, G.; Govindaraj, P.; Asokamani, A.; Suwas, S. Effect of Texture and Grain Size on Bio-Corrosion Response of Ultrafine-Grained Titanium. *Metall. Mater. Trans. A* **2013**, *44*, 5602–5610. [CrossRef]
92. Rifai, M.; Miyamoto, H.; Fujiwara, H. The Effect of ECAP Deformation Route on Microstructure, Mechanical and Electrochemical Properties of Low CN Fe-20%Cr Alloy. *Mater. Sci. Appl.* **2014**, *5*, 568–578. [CrossRef]
93. Gebril, M.A.; Omar, M.Z.; Othman, N.K.; Mohamed, L.F. Effect of Equal Channel Angular Pressing Processing Routes on Corrosion Resistance and Hardness of Heat Treated A356 Alloy. *Sains Malays.* **2019**, *48*, 661–668. [CrossRef]
94. Argade, G.R.; Panigrahi, S.K.; Mishra, R.S. Effects of grain size on the corrosion resistance of wrought magnesium alloys containing neodymium. *Corros. Sci.* **2012**, *58*, 145–151. [CrossRef]
95. Illgen, C.; Frint, P.; Gruber, M.; Volk, W.; Wagner, M.F.X. Evolution of Grain Refinement in AA5083 Sheet Metal Processed by ECAP. In *Light Metals*; Tomsett, A., Ed.; The Minerals, Metals & Materials Series; Springer: Cham, Switzerland, 2020; pp. 362–369. [CrossRef]

96. Cheng, W.; Tian, L.; Ma, S.; Bai, Y.; Wang, H. Influence of Equal Channel Angular Pressing Passes on the Microstructures and Tensile Properties of Mg-8Sn-6Zn-2Al Alloy. *Materials* **2017**, *10*, 708. [CrossRef] [PubMed]
97. Alateyah, A.I.; El-Garaihy, W.H.; Alawad, M.O.; El Sanabary, S.; Elkatatny, S.; Dahish, H.A.; Kouta, H. The Effect of ECAP Processing Conditions on Microstructural Evolution and Mechanical Properties of Pure Magnesium—Experimental, Mathematical Empirical and Response Surface Approach. *Materials* **2022**, *15*, 5312. [CrossRef] [PubMed]
98. Tolaminejad, B.; Dehghani, K. Microstructural characterization and mechanical properties of nanostructured AA1070 alu-minum after equal channel angular extrusion. *Mater. Des.* **2012**, *34*, 285–292. [CrossRef]
99. Alateyah, A.I.; Ahmed, M.M.Z.; Zedan, Y.; El-Hafez, H.A.; Alawad, M.O.; El-Garaihy, W.H. Experimental and Numerical Investigation of the ECAP Processed Copper: Microstructural Evolution, Crystallographic Texture and Hardness Homogeneity. *Metals* **2021**, *11*, 607. [CrossRef]
100. Lyszkowski, R. Influence of Strain Route Changes on the Microstructure and Mechanical Properties of CuZn36 Alloy during Cross Channel Extrusion CCE. *Materials* **2022**, *15*, 1124. [CrossRef] [PubMed]
101. Alateyah, A.I.; El-Shenawy, M.; Nassef, A.; El-Hadek, M.; Ahmed, M.M.Z.; Kouta, K.; El Sanabary, S.; El-Garaihy, W.H. Optimizing the ECAP processing parameters of pure Cu through experimental, finite element, and response surface approaches. *Rev. Adv. Mater. Sci.* **2023**, *62*, 20220297. [CrossRef]
102. Irfan, O.M.; Al-Mufadi, F.; Al-Shataif, Y.; Djavanroodi, F. Effect of Equal Channel Angular Pressing (ECAP) on Erosion-Corrosion of Pure Copper. *Appl. Sci.* **2017**, *7*, 1250. [CrossRef]
103. Del Valle, J.A.; Carreño, F.; Ruano, O.A. Influence of texture and grain size on work hardening and ductility in magnesi-um-based alloys processed by ECAP and rolling. *Acta Mater.* **2006**, *54*, 4247–4259. [CrossRef]
104. Wang, Y.; Chen, M.; Zhou, F.; Ma, E. High tensile ductility in a nanostructured metal. *Nature* **2002**, *419*, 912–915. [CrossRef] [PubMed]
105. Jin, H.; Lin, D.L.; Mao, D.L.; Zen, X.Q.; Ding, W.J. Mechanical properties and microstructure of AZ31 Mg alloy processed by two-step equal channel angular extrusion. *Mater. Lett.* **2005**, *59*, 2267–2270. [CrossRef]
106. Meyer, L.W.; Hockauf, M.; Zillmann, B.; Schneider, I. Strength, ductility and impact toughness of the magnesium alloy az31b after equal-channel angular pressing. *Int. J. Mater. Form.* **2009**, *2*, 61–64. [CrossRef]
107. Agnew, S.R.; Horton, J.A.; Lillo, T.M.; Brown, D.W. Enhanced ductility in strongly textured magnesium produced by equal channel angular processing. *Scr. Mater.* **2004**, *50*, 377–381. [CrossRef]
108. Naik, G.M.; Narendranath, S.; Kumar, S.S.S. Effect of ECAP Die Angles on Microstructure Mechanical Properties and Corrosion Behavior of AZ80 Mg Alloy. *J. Mater. Eng. Perform.* **2018**, *28*, 2610–2619. [CrossRef]
109. Paleyes, A.; Urma, R.G.; Lawrence, N.D. Challenges in deploying machine learning: A survey of case studies. *ACM Comput. Surv. (CSUR)* **2022**, *55*, 1–29. [CrossRef]
110. Blythman, R.; Arshath, M.; Smékal, J.; Shaji, H.; Vivona, S.; Dunmore, T. Libraries, Integrations and Hubs for Decentralized AI using IPFS. *arXiv* **2022**, arXiv:2210.16651.
111. Abid, A.; Abdalla, A.; Abid, A.; Khan, D.; Alfozan, A.; Zou, J. Gradio: Hassle-free sharing and testing of ml models in the wild. *arXiv* **2019**, arXiv:1906.02569.
112. Gradio Documentation. Available online: https://www.gradio.app/docs/ (accessed on 9 February 2023).
113. HuggingFace. Available online: https://huggingface.co/ (accessed on 9 February 2023).